Hyperspectral Imaging as a Tool for Characterization of Multicrystalline Silicon Wafers
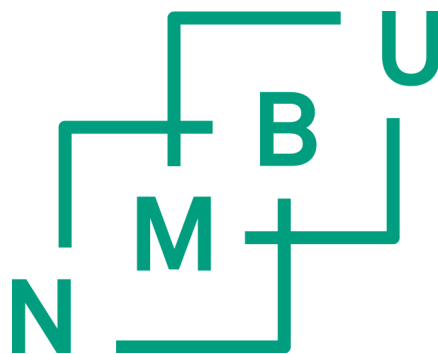
Hyperspektral avbildning som et verktøy for karakterisering av multikrystallinske skiver av silisium

Philosophiae Doctor (PhD) Thesis

Andreas Svarstad Flø

Department of Mathematical Sciences and Technology
Faculty of Environmental Sciences and Technology
Norwegian University of Life Sciences

Ås 2014

Summary

This thesis describes the development of a method for characterization of multicrystalline silicon wafers based on hyperspectral imaging. The aim has been to show the distribution of radiative defects in silicon wafers. Commonly used methods are often time consuming and destructive or based on indirect measurements. Hyperspectral imaging is a fast, non-destructive method which measures the distribution of radiative defects directly.

The exact mechanisms of the radiative defects are still not fully understood, but by using hyperspectral imaging in addition to complementary measurements, new knowledge of their origins can be obtained.

One issue in this thesis has been to show the possibilities of using hyperspectral imaging to visualize radiative defects. In combination with multivariate curve resolution we can quickly extract the weak signals from the raw hyperspectral images.

A research facility for cooled hyperspectral photoluminescence imaging, has in parallel with the experiments, been developed and tested. The laboratory consists of two hyperspectral cameras, excitation source and two cryogenic coolers.

50 wafers from a silicon block have been studied using the hyperspectral imaging setup. Additionally, RGB images, conventional photoluminescence images and interstitial iron mapping have been acquired. The different datasets have been preprocessed and corresponding points were located in all image types before an affine transform was performed to align them to a common coordinate system. Selected spectral defects were used to make 3D visualization to show the distribution of defects through the silicon block.

Sammendrag

Denne avhandlingen beskriver utviklingen av en metode for karakterisering av multi-krystallinske silisiumskiver basert på hyperspektral avbildning. Målet har vært å vise utbredelsen av de forskjellige luminiserende defektene som er gjeldende i silisiumskiver. Dagens metoder for karakterisering av silisium er ofte tidkrevende, destruktive eller er indirekte målinger. Hyperspektral avbildning er en rask og ikke destruktiv målemetode som måler den radiative delen av defektene fra silisium direkte.

Den fysiske årsaken til de radiative defektene er fortsatt ikke helt forstått, men ved å sammeligne hyperspektrale data med alternative målemetoder kan vi få en bedre forståelse om årsakene.

Et aspekt ved denne avhandlingen er å vise hvilke muligheter det gir å bruke hyper-spektralt kamera til å avbilde luminiserende defekter. I kombinasjon med multivariat statistikk kan en raskt ekstrahere de svake signalene fra defektene i bildene.

Det er parallelt blitt utviklet og testet en forsøksrigg for hyperspektral fotoluminesens med mulighet for kjøling av prøvene ned til 80K. Oppsettet består av to hyperspektrale kamera, en linjelaser og to kjølte prøveholdere. 50 skiver fra en silisiumblokk er blitt studert med prøveoppsettet. I tillegg er det tatt fargebilder, konvensjonelle fotolumine-sensbilder og utført måling av interstitielt jern av prøvene. De forskjellige datasettene er blitt preprosessert og felles punkter ble lokalisert i alle bildene før det ble kjørt en affin transformasjon for å gjøre bildene sammenlignbare. Utvalgte spektrale defekter ble valgt ut til en 3D visualisering for å vise utbredelsen gjennom silisiumblokken.

Acknowledgements

Contents

Abbreviations

BB	**B**and to **B**and
CDI	**C**arrier **D**ensity **I**maging
DLTS	**D**eep **L**evel **T**ransient **S**pectroscopy
DRL	**D**efect **R**elated **L**uminescence
EL	**E**lectro**L**uminescence
GDMS	**G**low **D**ischarge **M**ass **S**pectroscopy
HgCdTe	Mercury Cadmium Telluride
ICA	**I**ndependent **C**omponent **A**nalysis
IDLS	**I**njection **D**ependent **L**ifetime **S**pectroscopy
InGaAs	Indium Gallium Arsenide
MCR	**M**ultivariate **C**urve **R**esolution
MW-PCD	**M**icrowave **P**hoto **C**onduction **D**ecay
OD	**O**ptical **D**ensity
PCA	**P**rincipal **C**omponent **A**nalysis
PL	**P**hoto **L**uminescence
QSSPC	**Q**uasi **S**teady **S**tate **P**hoto **C**onductance
QSSPL	**Q**uasi **S**teady **S**tate **P**hoto **L**uminescence
SEM	**S**canning **E**lectron **M**icroscope
SIFT	**S**cale **I**nvariant **F**eature **T**ransform
SRH	**S**hockley **R**ead **H**all
TDLS	**T**emperature **D**ependent **L**ifetime **S**pectroscopy
TEM	**T**ransmission **E**lectron **M**icroscope

Chapter 1

Introduction

1.1 Motivation

The solar cell market is influenced by a strong competition in reducing the production cost. Multicrystalline silicon wafer technologies still dominate the market in the photovoltaic industry with approximately 80% market share [1], due to their low cost compared to alternative technologies such as mono crystalline silicon wafers and multi-junction cells. However, a variety of defects can occur in the silicon material, including the inclusion of metallic particles or structural imperfections of the silicon lattice. The presence of such material defects in the silicon material leads to a reduction in the photovoltaic conversion efficiency [2]. Much effort is therefore dedicated to understand how crystal imperfections in multicrystalline silicon appear, how they influence the cell efficiency and not the least, how they can be avoided or reduced.

It is not only the amount of defects that influences the efficiency of the solar cell, but also their spatial distribution in the silicon wafer. For example, evenly distributed metal impurities lead to high loss in the cell efficiency. Fortunately, most metal impurities are located at grain boundaries of the silicon crystals or they appear in clusters within the crystal. This concentration of impurities has the advantage that a sufficient lifetime of excited charge carrier may remain in the bulk silicon, allowing a high efficiency of the solar cell. It is therefore important to study the spatial distribution of relevant impurities in a wafer with the aim of improving wafer sorting.

Hyperspectral luminescence imaging is a fast non-destructive method that can be used to visualize both the spatial distribution and the spectral characteristics of the material defects in silicon. Hence this technology provides an opportunity to introduce individual preprocess handling at the wafer level, based on type of defects, in order to increase the quality of the final cells.

The following thesis investigates the use of hyperspectral imaging to detect radiative emissions from silicon wafers, with the aim of characterizing radiative defects. The first step was to clarify if it was at all possible to detect radiative emissions from the sub band gap in silicon by using hyperspectral imaging techniques. Secondly, a method was developed for hyperspectral photoluminescence imaging of cooled samples, and subsequent extraction of images of radiative defects in silicon, with the aim of increasing current knowledge of the different emission bands. The developed method was then applied on a larger set of commercial wafers, to study the distribution of radiative defects through the height of a silicon ingot.

The thesis is organized as follows. A brief introduction to the physics behind photoluminescence in silicon is given in Section 1.2. Section 1.3 gives an overview of the luminescence techniques commonly used to characterize radiative defects in solar cells and a short overview of the defect related luminescence signals. Chapter 2 describes the development of a novel method for hyperspectral imaging, able to detect luminescence from recombination processes through traps in solar cells. The results of the thesis are discussed in Chapter 3 and the main conclusions and suggestions for further work are presented in Chapter 4.

The following four papers are included in this thesis:

- Paper I: Spectral and spatially resolved imaging of photoluminescence in multicrystalline silicon wafers (2011) in Applied Physics Letters, 99, 011903.

- Paper II: On the origin of inter band gap radiative emission in crystalline silicon (2012) in AIP Advances 2, 042135.

- Paper III: Characterization of silicon wafers for photovoltaic applications using hyperspectral imaging (in review).

- Paper IV: Distribution of radiative crystal imperfections through a silicon ingot (2013) in AIP Advances 3, 112120.

1.2   A brief introduction to Silicon physics related to defects

The silicon crystal lattice can be illustrated as a large number of atoms bonded together with covalent forces. The silicon atom will make a covalent pair with four neighboring atoms in order to create a stable crystal structure as shown in Fig. 1.1a.
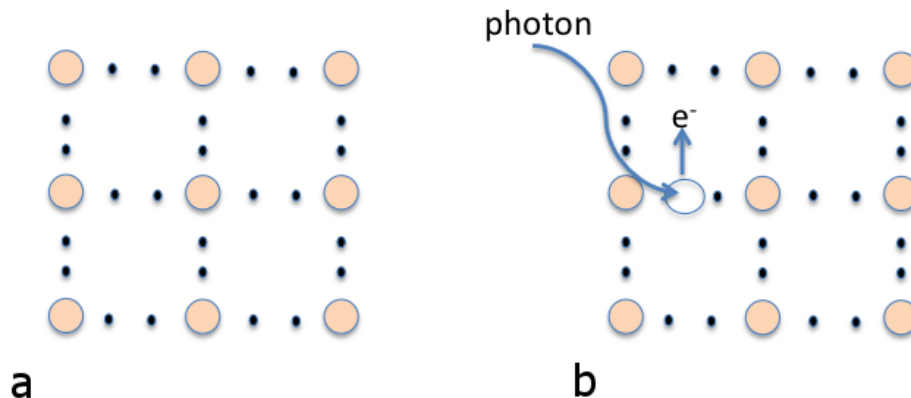
FIGURE 1.1: Illustration of the silicon crystal lattice. The circles denote the Si atoms while the valence electrons are shown as black dots. (a) All the electrons are paired. (b) An incident photon with high enough energy to brake the bond has created a free electron and a hole.

If a photon with high enough energy to break the electron pair binding interacts with an electron, the binding will break and the electron is free to move in the lattice. The electron with the corresponding hole, shown in Fig. 1.1b, is called an electron-hole pair. The free electron is not in a stable state and tends to recombine with a positive hole. The average time from an electron leaves a hole until it recombines is called the lifetime of the electron-hole pair. In order to generate electricity in an external circuit, the positive and negative charges need to be separated. This is achieved by doping the silicon either with atoms with one electron more than silicon, n-doped (n for negative doped) or atoms with one electron less than silicon, p-doped (p for positive). This introduces a so-called pn-junction and an electric field gradient, where the electrons and the holes are separated [3]. Electrons associated with single atoms have well defined sets of discrete energy levels available to them. In a crystal structure these energy levels are spread out into bands of allowed energy [4]. Energy bands allowed for electrons are separated by a bandgap, which is called the forbidden bandgap. For a highly pure silicon semiconductor there are no energy levels available for electrons within the forbidden bandgap. Silicon in a

crystal structure has a bandgap defined by:

$$E_{gap} = E_C - E_V \tag{1.1}$$

where E_C and E_V are the energy levels of the bottom of the conduction band and the top of the valence band, respectively.

When crystal faults or foreign atoms are introduced into the silicon crystal, they may give rise to energy states for electrons in the otherwise forbidden bandgap. Impurities, especially those which introduce energy levels near the middle of the bandgap leads to increased recombination of electron-hole pairs [4], thereby reducing the lifetime.

1.2.1 Defects and impurities in silicon wafers

Several types of material defects can be found in multicrystalline silicon (mc-Si). Mc-Si consists of a large number of grains, which are separated by grain boundaries. Each grain is a single crystal as shown in Fig. 1.2.
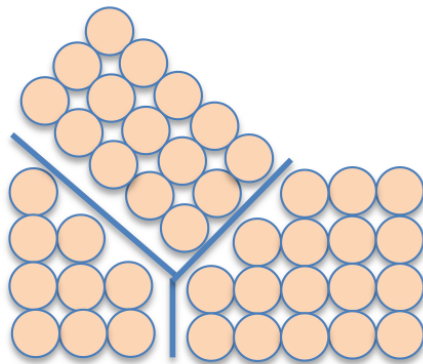
FIGURE 1.2: Illustration of the silicon crystal lattice with grain boundaries. The grain boundaries are the borders between the different crystals in the silicon.

The structural lattice defects may be classified into categories according to their geometry. These categories can be point defects, line defects, area defects and volume defects. Point defects can be a missing atom, known as a vacancy defect or an extra atom in a non-lattice site in the crystal, known as an interstitial defect as illustrated in Fig. 1.3.
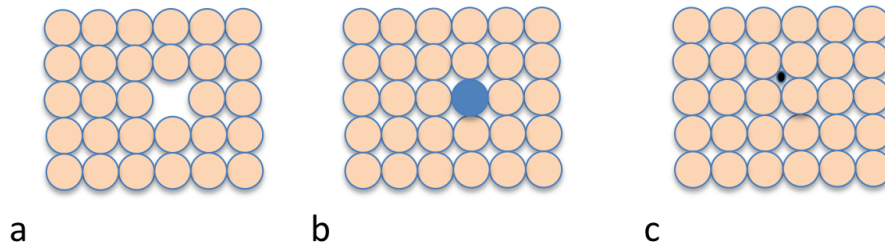
FIGURE 1.3: Illustration of point defects in the silicon crystal lattice. The circles denote the Si atoms. (a) A missing Si atom in the lattice, also called vacancy defect. (b) A substitutional impurity atom in the lattice. (c) An interstitial impurity atom in the lattice.

Line defects are known as dislocations. The dislocations can be divided into two groups: edge dislocations and screw dislocations [5, 6]. The types of dislocations are illustrated in Fig. 1.4. An edge dislocation contains an extra half plane, squeezed into the lattice. If the the dislocation forms a step or ramp it is referred to as a screw dislocation. During solidification and cooling process, material stress will introduce slip lines, where two parts of the crystal slides according to each other [6]. These material defects may act as recombination sites for electrons and holes reducing the minority carrier lifetime in the silicon wafers, and thus reducing the performance of the final solar cells [2].
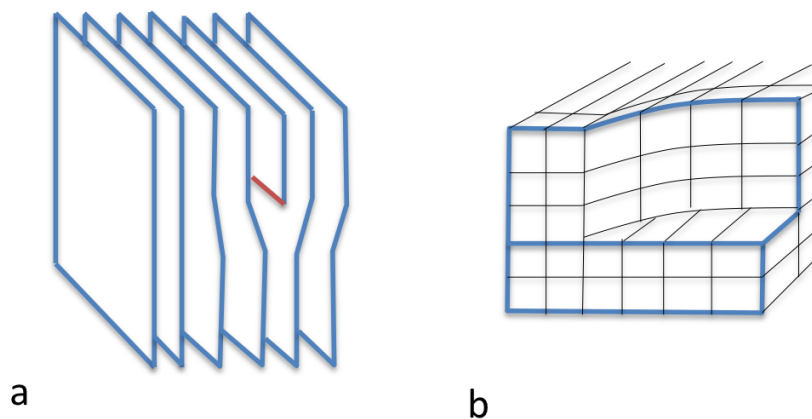
FIGURE 1.4: Illustration of dislocations. (a) Edge dislocation with an extra half plane. (b) Screw dislocation where two parts of the lattice has an rotation.

There are two categories of impurities in crystalline silicon [7]. One category is intentionally added dopants to modulate resistivity in the wafer material. The other one is unwanted contaminants. The sources of contamination in the production of multicrystalline silicon are the feedstock, the crucible, the coating of the crucible and the furnace.

Typical contaminants are C, O, N, Al and transition metals. The main metallic impurities are Iron, Nickel, Copper and Molybdenum. Iron can either exist as interstitial iron Fe_i or as a complex with other defects. In p-type mc-Si wafers, the interstitial iron is positively charged and tends to form pairs with other defects. Iron can form more than 30 different complexes. One of the most important complexes is Iron-Boron (FeB)[8]. The role of the different metals behavior in silicon has been extensively studied by Graff [9]

1.2.2   Recombination mechanisms in silicon

The main recombination mechanisms in silicon are Radiative band-to-band recombination, Auger recombination, Recombination through traps, also called Shockley-Read-Hall (SRH) recombination and Surface recombination [4]. These mechanisms are illustrated in Fig. 1.5.
Total recombination lifetime τ_{eff} is given by:

$$\frac{1}{\tau_{eff}} = \frac{1}{\tau_{SRH}} + \frac{1}{\tau_{Auger}} + \frac{1}{\tau_{rad}} + \frac{1}{\tau_{surface}} \qquad (1.2)$$

In the present thesis, recombination through traps is of special interest since this mechanism can result in luminescence from crystal imperfections [10], which can be measured using hyperspectral imaging technology. This will be further described below.

Radiative band-to-band

Radiative recombination is the reverse of the light absorption process. An electron in the conduction band makes a transition to the valence band and emits the difference in energy as light, as shown in Fig. 1.5a. The energy of the emitted photon corresponds to the bandgap of silicon, which is 1.124 eV. The emission from this process is denoted band-to-band luminescence.
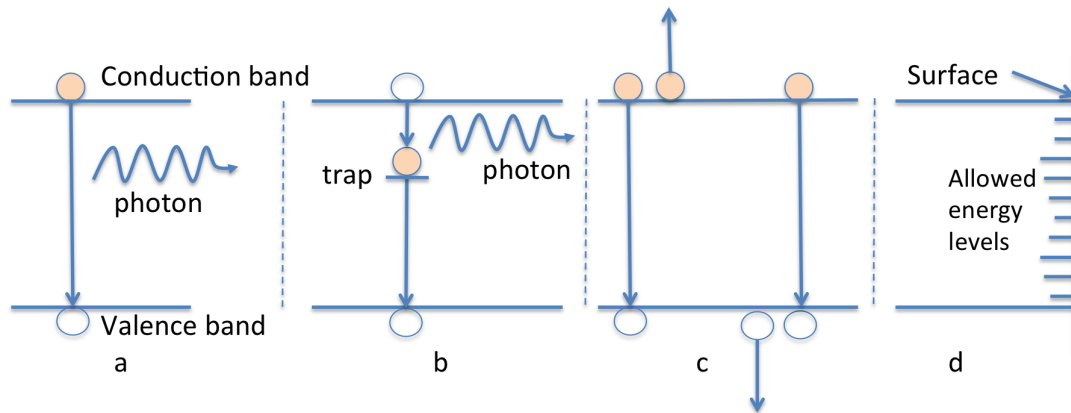
FIGURE 1.5: Schematic diagram of the recombination processes. (a) Radiative band-to-band recombination is where an electron from the conduction band combines directly with a hole in the valence band and releases a photon. (b) Recombination through traps is where an electron is trapped by an energy level within the forbidden bandgap, caused by defects. (c) Auger recombination involves three carriers. An electron and a hole recombine, but instead of emitting the released energy as heat or a photon, it is given to a third carrier. (d) Surface recombination is where the discontinuity in the crystal with unpaired bonds gives rise to a continuum of active levels in the bandgap.

Recombination through traps

Impurities and crystal defects can give rise to allowed energy levels, so-called traps, in the otherwise forbidden bandgap, as illustrated in Fig. 1.5b. The defect levels introduce a very efficient recombination process where electrons relax from the conduction band to the defect level(s) and then relax further to the valence band. The energy is released either as photons or phonons. Since the phonon activity decreases with lower temperature, the rate of radiative recombination through traps increases [4]. The emission from this process is in this thesis denoted Defect Related Luminescence (DRL).

Auger recombination

The Auger process is a three-particle interaction where the energy released by the recombination of an electron-hole pair is transferred to a third free carrier, which then releases its excess energy as phonons (thermalization), as illustrated in Fig. 1.5c. The third carrier can be either an electron in the conduction band or a hole in the valence band [11].

Surface recombination

The surface of silicon represents a discontinuity in the crystal structure, which leads to a large quantity of partially bonded atoms. These so-called dangling bonds, give rise

to recombination active levels within the bandgap, as illustrated in Fig. 1.5d. Unlike the recombination through traps, the surface recombination does not normally occupy a single energy level, but is distributed throughout the bandgap [11]. To minimize the effect of surface recombination, the surface of silicon wafers can be passivated with e.g. amorphous silicon [12].

Temperature dependence

The intensity of the radiative SRH recombination varies with temperature [13]. The intensity of the emissions from the inter bandgap generally become stronger at lower temperatures. These emissions have been studied in the range 4 - 300 K and the signals appears as separate signals below 100 K [14].

1.2.3   Luminescence

Luminescence from silicon can occur by three different phenomena: Electroluminescence (EL), where the electrons are excited by an electric current [15], cathodoluminescence, where the electrons are excited by an electron beam, and photoluminescence [16] where the electrons are excited by photons. Photoluminescence (PL) is defined as emission of light from a material after absorption of photons and is due to energy exchange within the material. The photoluminescence spectrum provides the transition energies, which can be used to determine electronic energy levels [16].

The intensity of the band-to-band PL signal has mainly been used in studies for wafer characterization. It is generally found that a high PL signal correlates with good solar cell properties. It is important to take into account the quality of the surface passivation [17, 18]. The recombination at the surface is usually non-radiative and reduces the band-to-band PL intensity.

The choice of excitation source will have an influence on the luminescence spectra. A laser is often used as an excitation source for PL, since it is monochromatic. Because the absorption in silicon depends on energy, the penetration depth of the laser will depend on its wavelength. Silicon is transparent for photons with energy lower than the bandgap. The absorption coefficient α determines how far light at a particular wavelength can penetrate into silicon before it is absorbed. The laser used in this work with wavelength 808nm has an average penetration depth of 13 µm at 300K according to the results by Green and Keevers [19]. The intensity of the excitation source controls the density of the photo-excited electrons and holes.

The average distance a carrier can move before it recombines is called the diffusion length. The diffusion length is related to diffusivity and carrier lifetime and is defined as:

$$L = \sqrt{D\tau} \tag{1.3}$$

where L is the diffusion length in meters, D is the diffusivity in m^2/s and τ is the lifetime. This effect leads to a blurring of the images in areas where lifetime is high.

Sub bandgap photoluminescence

There are several other radiative emission mechanisms in silicon in addition to the band-to-band recombination. Four radiative emission lines, believed to originate from recombination related to dislocations in the crystals were first reported by Drozdow et al. in 1976 [10]. These four lines are conventionally labeled D1, D2, D3 and D4 with energies 0.8 eV, 0.87 eV, 0.94 eV and 1.0 eV, respectively. A typical spectrum showing the D-bands is shown in Fig. 1.6.
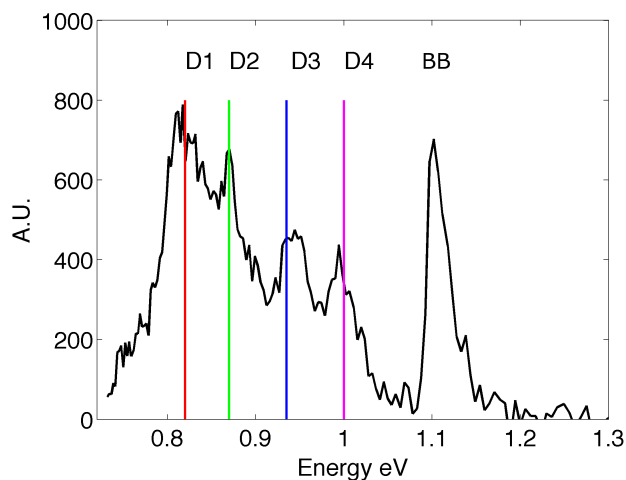
FIGURE 1.6: A typical defect related luminescence spectrum, extracted from a point on a mc-Si wafer used in paper II. It clearly shows the different emission peaks D1-D4 in addition to the band-to-band luminescence.

Several theories have been proposed for the origins of the D-lines and other radiative emissions from crystal imperfections, also called Defect Related Luminescence (DRL). Sauer et al. [20] suggested that D1-D4 are due to relaxed dislocations. Higgs et al. [21] suggest transition-metals as a source for the D-band emission lines. Further, it has been proposed by Ostapenko et al. [22] that oxygen or heavy metals influence the half-width and intensity of D1. Sekiguchi and Sumino [23] associate D3 and D4 with slip lines and link D1 and D2 to intersections of plural slip lines. They also observed pairwise similarity between D1/D2 and D3/D4 regarding their spatial distribution. Oxygen precipitates

have also been found to be a possible origin of the D-lines [24]. D3 and D4 have been linked to dislocations decorated by metallic impurities by Arguirov [12]. Recently Mchedlidze et al. [25] associate screw dislocation with a small twist angle to the D-lines whereas the edge dislocations were associated with non-radiative recombination.

A strong emission at 0.93-0.94 eV, different from D3, has been attributed to Sulfur by Brown and Hall [26] and recently Krause et al. [27] relate the signal to dislocation network formed at $\sum 3$ grain boundaries.

1.3 Characterization of recombination active defects in mc-Si

Several methods exist for characterizing defects in mc-Si wafers. They can be divided into two general categories: point based techniques, where one point or an area is measured, and imaging based techniques.

1.3.1 Point based and scanning based methods

Microwave photo conductance decay (MW-PCD) uses a laser as the excitation source, which causes a change in the conductivity of the wafer. The change in conductivity is measured by reflected microwaves and carrier lifetime is calculated [28]. This is a point based measurement technique, but it can scan over the sample and provide a spatial life-time map. Deep-level transient spectroscopy (DLTS) was first described in 1974 by Lang [29]. This method measures the capacitance transient changes in the depletion layer of a p-n junction associated with a bias pulse as a function of temperature in a single point. It has the capability to measure non-radiative traps in addition to the radiative centers visible with photoluminescence techniques. This is considered to be a highly sensitive technique to detect and analyze small concentrations of electrically active defects. More recently other spectroscopic techniques have been developed such as injection dependent lifetime spectroscopy (IDLS) and temperature dependent lifetime spectroscopy (TDLS) [11]. These techniques are based upon a MW-PCD setup with a sample holder with a cryostat and an adjustable illumination source to obtain the temperature and injection dependency on small samples. TDLS and IDLS extract more information from the wafers by studying both temperature dependence and injection dependence on the PL signal. Another method is luminescence spectroscopy as described by Ostapenko and Schubert et al.[22, 30]. This method uses a laser as excitation source and a spectrometer to obtain the luminescence spectrum.

The Quasi-steady-state photo conductance (QSSPC) uses a photographic flash lamp as

the excitation source. The wafer is inductively coupled by a coil to a high-frequency bridge, which detects the changes in the conductance. A reference solar cell and an oscilloscope are used to determine the time dependence of both the excess photo conductance and the illumination. The lifetime can be determined by using appropriate calibration functions [11]. This is a point measurement which result in an average lifetime over the area of the coil.

There are many other techniques which can be used to determine the contamination content in silicon at selected points. Cathodoluminescence [23], often connected to a microscope, provides high resolution, but over a limited area. Fourier transform infrared spectroscopy (FTIR) can be used to measure oxygen content in silicon wafers [24]. Glow Discharge Mass Spectrometry (GDMS) [31], is a point based measurement, which can detect low concentrations of impurities [32]. There are many possibilities using electron microscopes such Scanning Electron Microscope (SEM) [33] and Synchrotron [30, 34] and Transmission Electron Microscopy (TEM) [35]. Synchrotron techniques with X-ray fluorescence [30, 34] provide measurements of the chemical composition, but do not involve the physical principle of generation/recombination of electron hole pairs.

1.3.2 Imaging methods (camera based)

The intensity of the general broadband emission of luminescence for wafers is commonly measured in PL imaging techniques. The use of PL imaging for silicon wafers has developed rapidly in recent years due to its speed, non-destructive nature and its simplicity regarding instrumentation. Standard camera based luminescence techniques are widely used [18, 36, 37]. PL imaging has several advantages. It has high spatial resolution, the cameras are inexpensive and the acquisition time is short enough for inline use [38].
To calculate carrier lifetime from the PL images, calibration is often performed with a QSSPC measurement [39, 40]. Recently, a method called Quasi-Steady-State Photoluminescence QSSPL was shown by Giesecke et al. [41].

The PL imaging technique has been developed further for indirect measurements of the defect distribution. MacDonald et al. [42] describe a technique to calculate interstitial iron by using PL-images before and after dissociation of the iron-boron pair. Schubert et al. [43] has extended the technique to include other metastable defects such as boron-oxygen and chromium-boron.

Carrier Density Imaging (CDI) is a method using the change in transparency of silicon in the IR region due to excited electrons, to measure carrier lifetime using a thermographic camera. The method is proposed by Bail et al. [44]. This is a laboratory method

that requires two images to detect the lifetime, one with illumination and one without illumination.

Electroluminescence (EL) is an imaging technique which uses electricity to generate carriers and a CCD camera to capture the generated luminescence. There are mainly two types of images generated from EL, forward bias images and reverse bias images. Mankovic et al. 2012 [45] describe a tool to classify defects by using different excitation voltages using electroluminescence. EL is only applicable to finished processed solar cells, not to wafers.

The term defect related luminescence is used for methods studying radiative emissions from the sub bandgap. An example spectrum from a wafer used in this work is illustrated in Fig. 1.6, showing different defect related emissions. Recently, defect band luminescence with e.g. an InGaAs camera with band pass filters has been used for mapping the integral of wavelength over a range in the luminescence spectrum [45–49]. This method is based on similar cameras as our hyperspectral camera. It acquires an entire object at a time, so it is a fast method. The resulting image shows the spatial distribution of one part of the spectrum, whereas the hyperspectral technology provides all spectral features.

Hyperspectral imaging has been reported for spectrally resolved BB electro-luminescence by Peloso et al. [50, 51]. The authors suggest that the shape of the BB peak may reveal physical device parameters affecting the luminescence. Li et al. 2010 [52] describe a method for crack detection in Cz-Si solar cell, by analyzing the laser reflection. Recently, a thesis by Delamarre [53] using a hyperspectral camera connected to a microscope was published, studying CIGS thin-film solar cells.

Hyperspectral defect luminescence imaging provides an extra dimension in relation to the other luminescence based methods. Compared to luminescence spectroscopy [22, 30], this method adds a spatial dimension, which can visualize the distribution of the different emissions. Hyperspectral imaging reveals a detailed spectrum at each pixel, whereas defect band luminescence spectroscopy [45–49] gives an image integrated over a spectral range. The hyperspectral imaging method is non-destructive and may be used in different stages of solar cell production, from as-cut wafers to solar cells.

Chapter 2

Materials and methods

2.1 Development of a new method

This chapter describes the development of a new application of hyperspectral imaging technology, that has resulted in a novel method for characterization of silicon wafers. After a short introduction to the principles of hyperspectral imaging technology, I will describe how the imaging laboratory was designed for this application. I will also give a description of how the data were preprocessed and analyzed.

2.2 Hyperspectral imaging

Hyperspectral imaging combines spectral information and conventional imaging by recording a full spectrum in each pixel of an image [54]. There are mainly two types of hyperspectral cameras. One is a filter based system with either a tunable bandpass filter or filter wheel. This system records the entire scene/sample at once, one wavelength range per frame. The other type, referred to as push broom scanner [55],which is used in the present study, scans the sample line-by-line, at all the wavelength ranges at a time. Hyperspectral images are represented as data cubes, often called hypercubes. An example visualization of a hypercube is shown in Fig. 2.1a. The spatial information is collected in the X-Y plane, while the spectral information is represented in the Z plane.
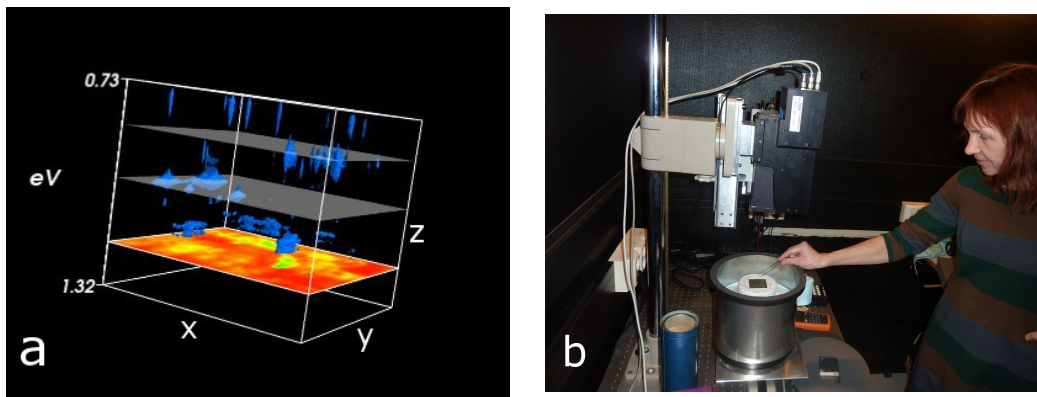
FIGURE 2.1: a) A 3D representation of a hyperspectral image of a mc-Si wafer. A band-to-band PL image is displayed in red-yellow and additional information from other channels in blue (defects in our sample). The x and y axes are the spatial directions and the z axis is the spectral/energy direction. b) Current setup with the NEO hyperspectral camera.

2.3   Instrumentation

The Dept. of Mathematical Sciences and Technology, Norwegian University of Life Sciences, started to establish and build an imaging laboratory in 2005. The first hyperspectral camera was acquired in 2007, an InGaAs camera SWIR 320i (Norsk Elektrooptikk AS, Oslo, Norway) with a spectral range 900-1700 nm. An example image and setup for the NEO camera is shown in Fig. 2.1. The camera provides 150 channels with 12 bit resolution. The NEO camera has fixed focus. To adjust the focus, the distance from the camera to the object must be changed.

The second camera is an HgCdTe SWIR camera (Specim, Spectral Imaging Ltd, Oulu, Finland) with a spectral range of 1000-2500 nm with 256 spectral channels and 14 bit resolution, and was acquired in 2011.

A flexible closed cabinet solution, shown in Fig. 2.2, was designed and built in black anodized aluminum to protect the samples from reflections and ambient stray light and to shield the users from laser reflections.
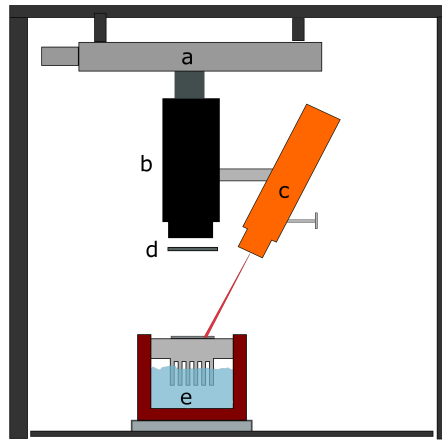
FIGURE 2.2: Current hyperspectral imaging setup in the hyperspectral laboratory with a) linear translation stage, b) Specim hyperspectral camera, c) illumination source (laser), d) long pass filter to prevent the light laser reflection to enter the camera optics, e) cryogenic cooler with sample holder. The system is enclosed in a cabinet.

2.3.1 Illumination

When studying PL signals, the recorded light is emitted by the sample, whereas in standard photography, it is the reflected light that is recorded. The luminescence signal is not visible to the naked eye, since it emits at NIR wavelengths. Moreover, it is very weak and can be difficult to extract from the noise level. The first experiments were performed with LED diodes as illumination source, as illustrated in Fig. 2.3a. The camera setup was easy to use since the entire object was illuminated at once. However, we were not able to create a homogeneous and reproducible light-field with this setup. An example image from this setup is shown in Fig. 2.3b. The image shows that the distribution of the photoluminescence was heterogeneous indicating that the illumination was not sufficiently homogeneous.
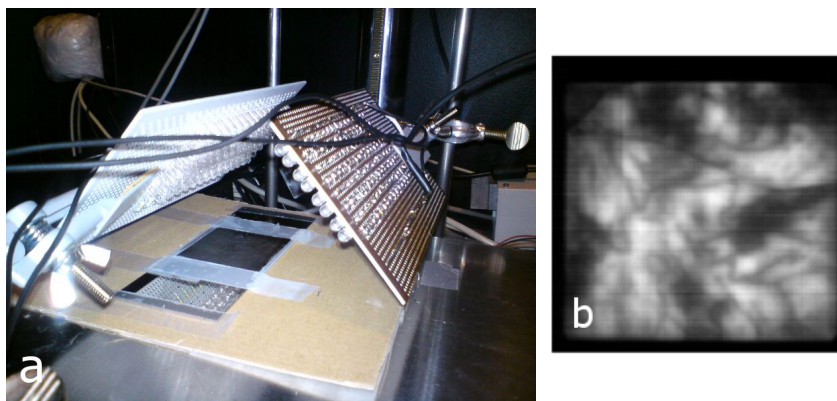

FIGURE 2.3: a) First experiment of hyperspectral imaging of silicon wafers. The excitation source consisted of LED diodes soldered on a PCB board. Photo: Odd Magnus Eng, b) PL image of a silicon wafer obtained using LED illumination. The image shows the heterogeneous distribution of the emitted photoluminescence.

A line laser at 808 nm (Solid state diode laser, 2 W) was therefore acquired to improve the homogeneity and intensity of the illumination source. The laser light is not recorded by the cameras, since they are sensitive in the wavelength region 900-2500 nm. To use a line laser, the laser line needs to be aligned along the camera's field of view. This was done by localizing the detectable line of the hyperspectral cameras and marking it. The laser was adjusted to the marked line. An illustration of the setup and a resulting image is shown in Fig. 2.4.
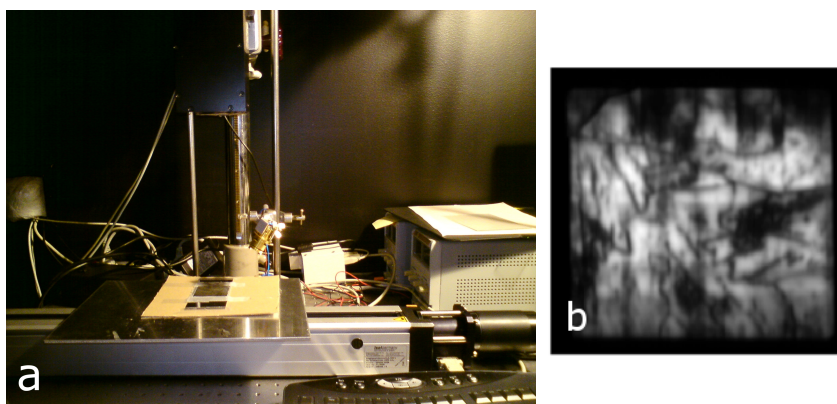
FIGURE 2.4: a) Experimental setup showing the hyperspectral camera and silicon wafers. Illumination source was a 2W line laser, b) PL image of a silicon wafer obtained using laser illumination.

The resulting image (Fig. 2.4b) from the laser setup showed better contrast and higher signal compared to the LED setup (Fig. 2.3). However the intensity profiles of this laser were not stable. Furthermore, the line was not homogeneous showing a Gaussian like shape, with a stronger signal towards the center of the line. Therefore, a new, more powerful laser (Lasiris Magnum II, 808 nm, 5 W, Gammadata Instrument AB, Uppsala, Sweden) with an irradiated power density of $2W/cm^2$ and a flat intensity profile was acquired. A goniometer and rotary stage with micrometer adjustment was obtained to simplify the laser alignment. The fine adjustment is performed with a wafer in place by maximizing the luminescence peak seen in the camera software. This setup provides a homogeneous intensity profile and an example image from this setup is shown in Fig. 2.5, showing higher intensity and acceptable homogeneity.
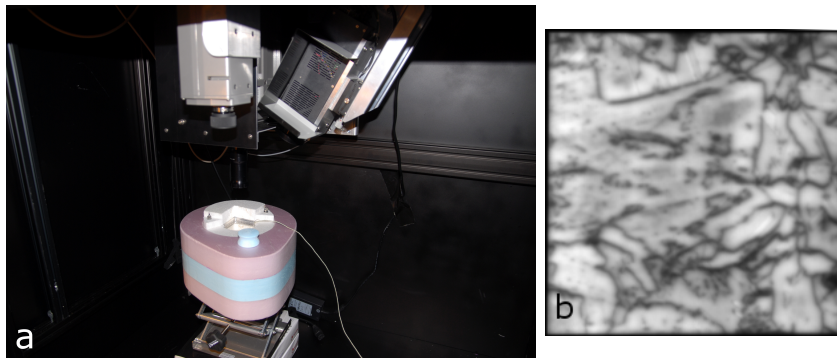
FIGURE 2.5: a) Experimental setup showing the Specim hyperspectral camera. The current illumination source was a 5W line laser. b) An example image of a silicon wafer from the current setup showing band-to-band luminescence.

2.3.2 Optics

Second order refraction from the illumination source gives an unwanted signal at 1616 nm in the recorded image. A 850 nm high performance long pass filter (Edmund Optics) was used to minimize this effect. The filter's blocking effect, the optical density (OD), is determined by the order of intensity that is blocked and can be calculated by:

$$OD = \log_{10} \frac{I_0}{I_T} \tag{2.1}$$

where I_0 is the initial intensity, and I_T is the transmitted intensity. The filter is specified to be OD≥4. Different filters were tested. It was found that filters with a sharp transition, as shown in Fig. 2.6, increased the image quality. The filter is placed at the camera lens (see Fig. 2.2).
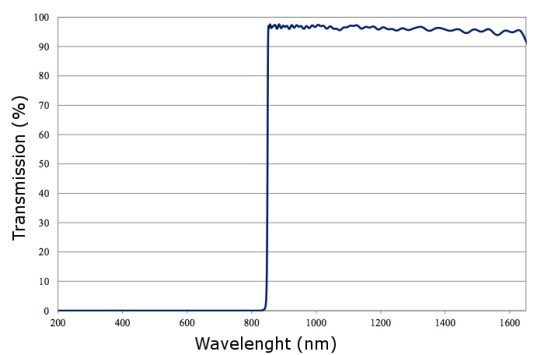
FIGURE 2.6: The transmission of the 850 nm high performance long pass filter. The filter blocks all wavelength less than 850 nm, including the laser's wavelength, but transmits light with higher wavelengths.

2.3.3 Temperature controller

During this work, two cryogenic sample holders were designed to enable cooling of the wafers to temperatures where the defect luminescence emissions was visible. The first one was designed with both cooling and heating capabilities and is illustrated in Fig. 2.7a. The cooler consisted of an inner steel cylinder with a removable cover of aluminum, referred to as the sample holder. The sample holder has small heating elements near the surface to control the exact temperature. It is also equipped with small holes for creating a vacuum, to hold the sample in place during the measurements. The cylinder is surrounded by 5 cm isolation. The barrel is filled with liquid nitrogen. The first version achieved temperatures from 110K - 340K.

The temperature of the cooled sample was still too high. The second cooler, as shown in Fig. 2.7b, was optimized such that lower temperatures could be achieved. The sample holder was made of one piece of aluminum with several cold fingers and purging of cold nitrogen gas over the wafer. This cooler can cool the wafer to 80K and is stable for several hours.
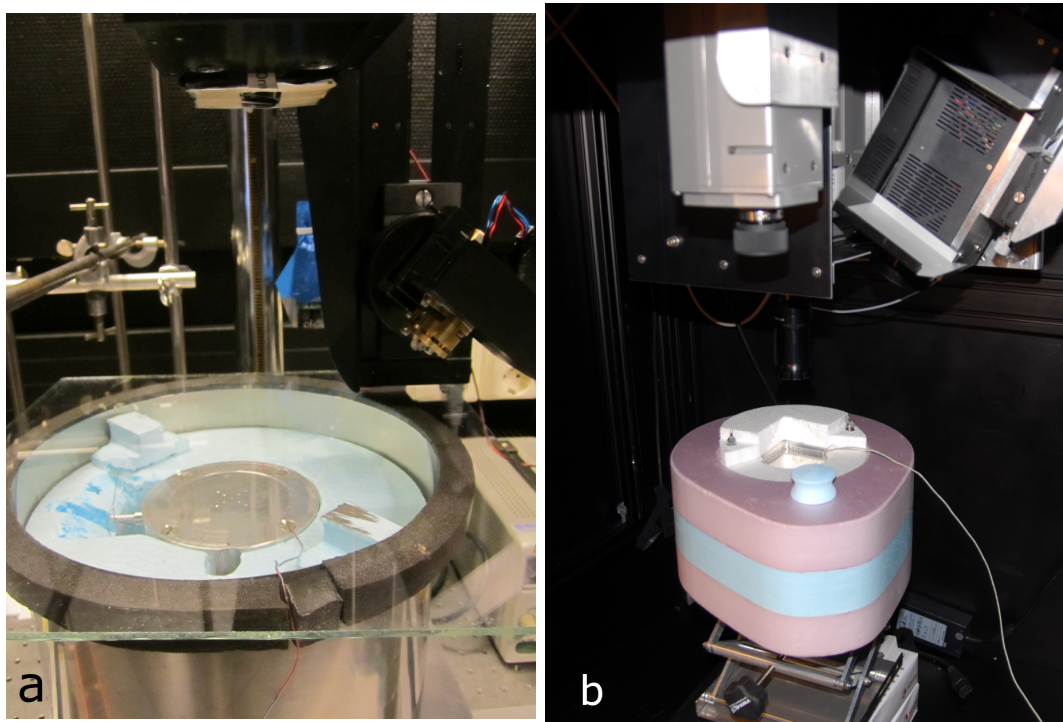

FIGURE 2.7: a) First version of the cryogen cooler with the sample holder shown in the middle. This cooler has, in addition to cooling, a system for creating a vacuum to hold the wafer and heating elements to adjust the temperature. b) Current version of the cryogen cooler with flushing of cold gas over the wafer.

2.3.4   Camera calibration

Calibration of hyperspectral cameras can be divided into several steps. First, the cameras response at different wavelengths is adjusted. This camera calibration is normally done by the vendors and the calibration factors are included in the software. A correction for the illumination profile spatially and spectrally is also important. In reflectance imaging, when the excitation spectrum is the same as the camera's spectral range, a reflectance standard should be used [54]. In luminescence imaging, the illumination wavelength is not detected by the camera. The laser is monochromatic and the wavelength is known, but the intensity profile is not always constant. One way to solve this issue was to find a homogeneous material with similar luminescent behavior as multicrystalline silicon. A mono-crystalline wafer was tested as reference to adjust the intensity variation of the illumination source. This was difficult due to the different luminescence intensity signals between the mono-crystalline and multicrystalline wafers. The difference in intensity between the sample and reference was so high that it was not possible to acquire it simultaneously with the same acquisition time. The current laser has a documented and even intensity profile. Another important issue is to validate the spectral calibration for the channels. This is often performed with different lasers and an integrating sphere or a lamp with spectral peaks such as a Hg lamp. The wavelength calibration from the camera vendor corresponded well with the findings of the so-called D-lines described in Papers II and III.

Absolute calibration is a method to calculate the absolute radiance detected by the camera. This is important when comparing two samples with respect to intensity of the defects. To be able to use the setup developed in this thesis to measure calibrated lifetime, an absolute calibration should be performed.

Recently a method for relative and absolute calibration for hyperspectral imaging of luminescence of wafers with a microscope by Delamarre was described, using a fiber optic cable mounted to the camera optics for the absolute calibration [56].

2.4   Data analysis

2.4.1   Preprocessing

The raw images from hyperspectral cameras appear more noisy than standard cameras. This is due to the fact that the signal is split into all the wavelength channels and thereby has less intensity per channel. The noise from detector variations can be reduced by subtraction of dark frames. The dark frames were obtained by closing the aperture and

capturing 100 frames with the same exposure time as the sample frames. These were averaged and subtracted from the raw frames. An additional step was added for the NEO camera to optimize the data. The NEO images show a wafer in the center surrounded by the aluminum surface of the sample holder, that is also seen as a background beneath the wafer. This background signal was subtracted by averaging the pixel columns on each side of the wafer for all spectral channels. This step did not improve the results on the images from the Specim camera.

2.4.2 Alignment

In order to compare the hyperspectral imaging method to other imaging techniques, aligning the different images was necessary. The first task was to align a hyperspectral image of a wafer taken at low temperature with an image taken at room temperature, in order to overlay an image with defect related luminescence over an image with BB luminescence, as shown in Paper III. The main issues were low contrast and difficulties in locating the corners of the wafer. High contrast images were created by summing together signals from selected channels. From these high contrast images it was possible to extract the coordinates of the corners of the wafer from the contrast images.
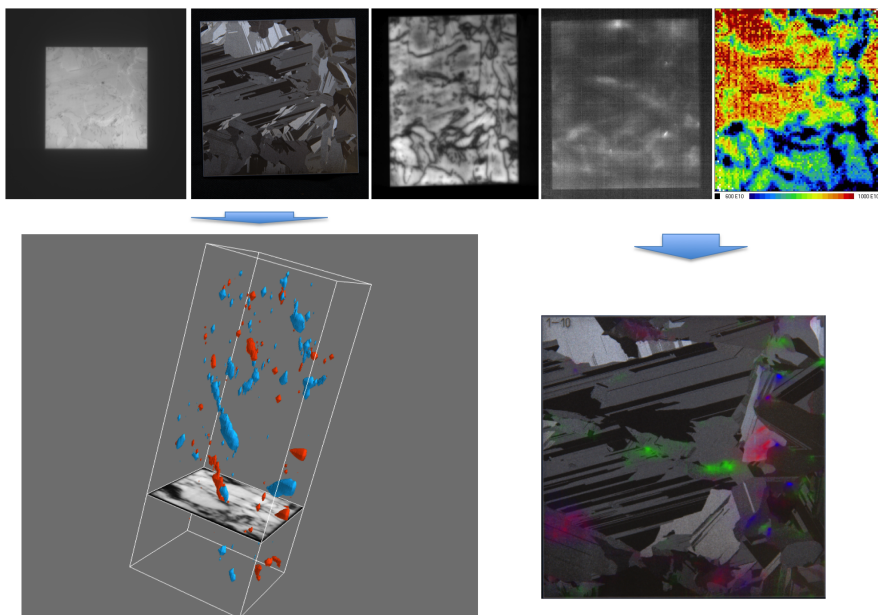
FIGURE 2.8: Alignment of five datasets of 50 wafers to one common coordinate system. Top) The five different datasets. (PL, RGB, hyperspectral PL, Defect related PL, and FeB). Left) The resulting 3D visualization of two different defects through the block. Right) Visualization of one wafer with a RGB image with defects overlaid.

A goal in Paper IV was to align data from 50 wafers (see Fig. 2.8) of the stack to a common coordinate system. Each wafer had five different measurements which should

be transformed. The datasets had different scales and different contrast as shown in Fig. 2.8. It was decided to use affine transform to account for translation, scaling, rotation and perspective changes [57, 58].

There were two reasons for developing an automatic approach for localizing corresponding points in images from different measurement techniques: i) the huge amount of data provided by the hyperspectral images and ii) an automatic algorithm will be more precise and reproducible.

FIGURE 2.9: a) Scorpion imaging automation software showing the method for edge detection. b) An example from the experiments using the automatic alignment method (SIFT).

Ideally, the alignment method should be fully automatic. Feature based alignment is an approach for detecting and extracting local feature descriptors that are reasonably invariant to changes in illumination, image noise, rotation, scaling, and small changes in viewpoint. One method within feature based alignment is Scale Invariant Feature Transform (SIFT) [59]. Thi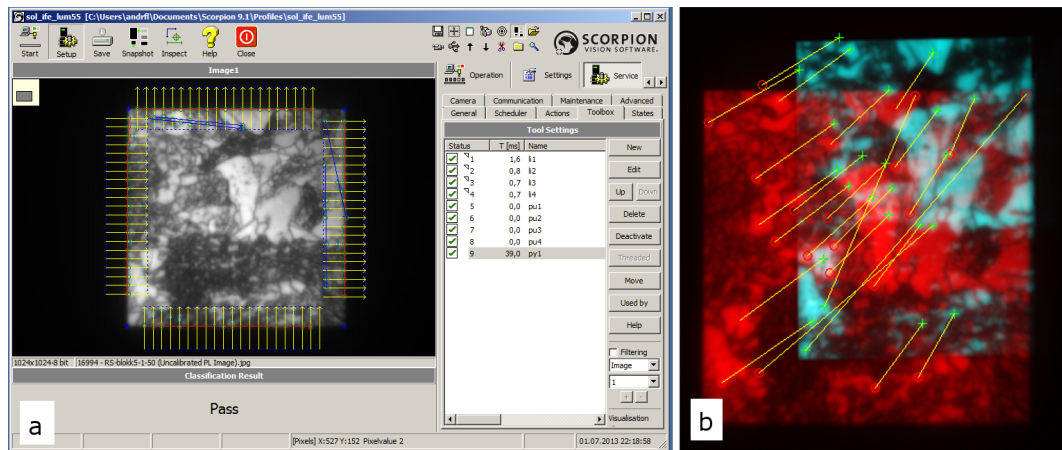s method was used successfully for aligning data from a few of the datasets of the same wafer as shown in Fig. 2.9b. Due to the low contrast and the shapes of the defect related luminescence, a more manual point detection method was chosen. A method for automatic corner detection was developed in Scorpion [60], a framework for vision automation, as illustrated in Fig. 2.9a. Contrast images were generated by summing the signals from selected wavelengths. The contrast images were imported to Scorpion. Edge detection functions were complemented with information about direction, position and threshold values. After the edges were localized, the corners were calculated as the crossing point of the edges and exported with Python. The corners were used as input for an affine transform in Matlab [61] to align the 3D cubes from the hyperspectral camera and complementary measurements into a common coordinate system. The workflow of the alignment method is shown in Fig. 2.10. For certain measurements, a manual selection of correspondence points was selected, because the signal and contrast at some of the edges were very low.
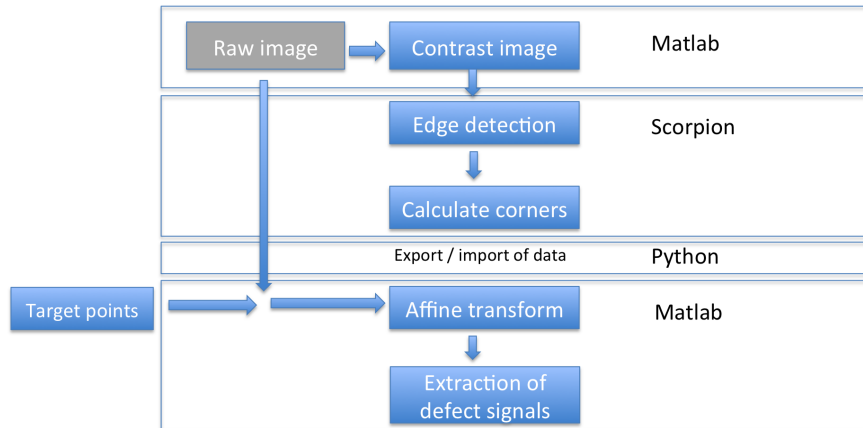
FIGURE 2.10: The workflow for the image alignment method for the hyperspectral images. A target point is chosen from one of the images. First, a contrast image is created in Matlab by adding signals from selected wavelength. This image is exported to Scorpion, an image automation software, where corners are detected. These coordinates are input for the affine transform in Matlab and applied on the hyperspectral image. The different selected emissions where extracted from the corrected image.

2.4.3   3D-visualization

The different aligned datasets were imported and processed in Matlab for creating data files for 3D visualization. Since each preprocessed image from the hyperspectral camera is over 600Mb, a script to traverse the 150 files and extract signals from the hypercube was needed. One 3D model file for each signal was created. Visualization software (Python [62] and Mayavi2 [63]) was used to combine the data files into a 3D model. When visualizing one sample, energy was set in the third dimension. For Paper IV one or two defects were displayed simultaneously with the height of the silicon block as the third dimension, as shown in Fig. 2.8 (left).

2.4.4   Multivariate analysis

Hyperspectral data often contain thousands of spectra, many of them highly correlated. There is a need for tools to extract the most significant information from the data. The signal from the crystal defects of interest in this thesis are very weak and often hard to distinguish from noise. We usually have some a priori knowledge about the signals we want to extract from silicon wafers. Since the underlaying physics and the interaction between the signals is unclear, much effort has been put into the interpretation of the solutions obtained from the different multivariate methods described below. To evaluate the chosen statistical method, manually extracted emission images from the D-bands and spectra from selected points were used. This is shown in Figure 6 in paper III.

Methods for signal extraction were considered. Principal component analysis (PCA) [64], independent component analysis (ICA) [65] and multivariate curve resolution (MCR) [66]. In this thesis the focus has been on MCR.

PCA is a variance method for reducing the dimensionality of large two-dimensional data sets. PCA finds a linear transformation of the original data into the orthogonal directions where variance is maximized [64]. Each principal component is composed of a loading vector and a score vector. The loading vector values represent the weights for each variable and represent the so-called latent variables. These are variables that contain the most important information in the data. The score vector contains the original data in the rotated coordinate system. Due to the orthogonality and the maximum variance constraint of PCA, it does not necessarily provide the concentrations and true spectra of the image constituents [67]. PCA applied to hyperspectral images has been used for bruise detection in mushrooms and apples [68, 69], which is quite similar to defect classification in silicon.

MCR is an iterative resolution method that strives to recover the pure spectra of an unresolved mixture when no prior information is available about the nature of the mixture of different spectra [67]. MCR is based on a bilinear model, which requires a linear combination of the spectra of the pure components in the system. The bilinear model is in the form

$$D = CSt + E \tag{2.2}$$

where D is the raw measurement, C is the matrix of concentrations, and St the matrix of related pure spectra. E is the experimental error contained in the raw measurement and is minimized using the alternating least square method [70]. For the work presented in this thesis MCR was implemented in PLS Toolbox 7.03 [71]. An example of MCR used on one of the wafers is shown in Fig. 2.11. Different constraints such as non-negativity [72] and unimodality [73] can be applied to the model. In the present study the data were mean centered and non-negativity constraints were applied. Two image applications of the MCR method are described by Juan et al. [74] where MCR used on spectral images of tablets with acetylsalicylic acid as the active compound and Gallagher et al. [75] used MCR to analyze drug images using secondary ion mass spectroscopy.

MCR works on two dimensional matrixes, so the 3D hypercubes were unfolded. After the analysis, the C matrix can be folded back to yield a map of concentration distributions of e.g. defects in silicon wafers.
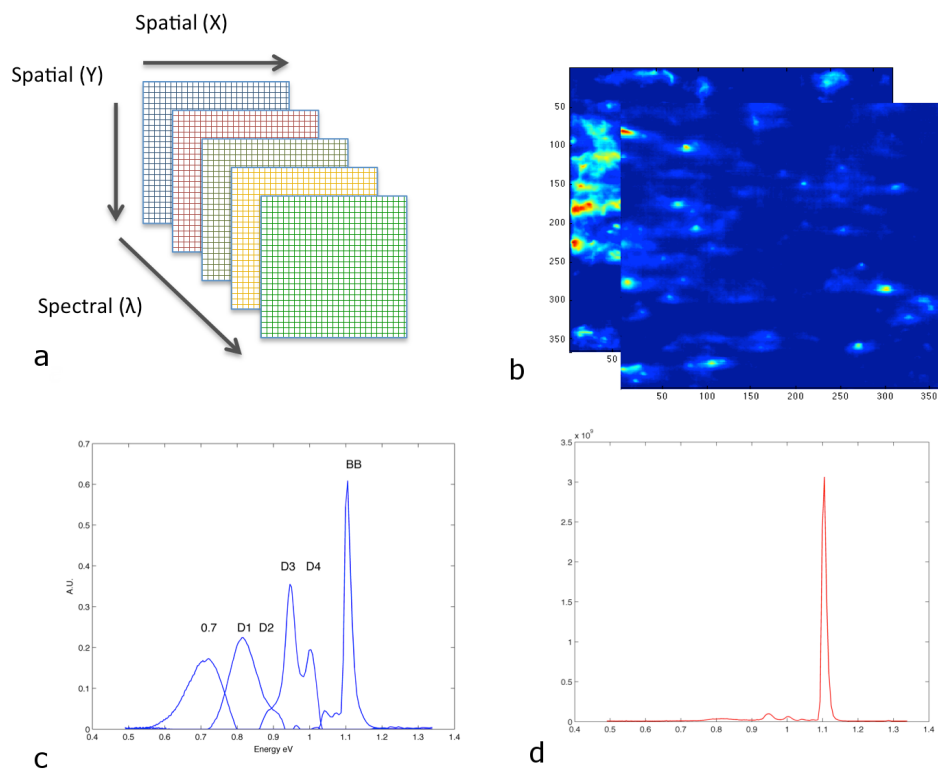
FIGURE 2.11: An example of MCR applied on a hyperspectral image. The images corresponds to Eq. 2.2. a) The hypercube of the wafer. b) The concentration images for the four components. c) The four extracted spectra, showing the different emissions. d) The residual spectra which is not modeled.

Chapter 3

Papers in this thesis

Paper I shows that it is possible to detect and distinguish between different defect related emissions from the sub bandgap of silicon in a cooled wafer using a hyperspectral InGaAs camera. Paper II compares these emissions to previously described emission lines detected by spectroscopic techniques. In Paper III, the goal was to use explorative multivariate analysis techniques to extract the signals present in the studied sample. Paper IV used this knowledge on a commercial set of wafers. In addition, a hyperspectral image alignment was performed to visualize the defect signal in a 3D model.

Paper I: Spectral and spatially resolved imaging of photoluminescence in multicrystalline silicon wafers

The first results of hyperspectral defect related luminescence imaging on Si wafers were reported in Paper I. Compared to commonly used methods for studying radiative defects in silicon, such as luminescence spectroscopy [22, 30], this method has many advantages. The method can show the distribution of defect related luminescence over a wafer, spectrally resolved, within the timeframe of approximately 5 seconds. Photoluminescence properties of the mc-Si wafers in the wavelength range 900-1700 nm in both the spatial and spectral dimension are discussed. Three radiative signals in addition to BB were observed with peaks at 0.81 eV, 0.94 eV and 0.97 eV. The signal at 0.81 eV showed a broad peak in the spectra, with high intensity in areas with low lifetime. This peak was also earlier observed by Koshka et al. [76]. A double peak with peaks at 0.94 eV and 0.97 eV was also observed. These two signals coexist in general, but the peak at 0.94 eV had some additional intense spots on the wafer. The peaks also showed a negative correlation to the BB-PL signal. Thus this paper demonstrated the possibilities of using a hyperspectral InGaAs camera for wafer characterization.

Paper II: On the origin of inter band gap radiative emission in crystalline silicon

In Paper II, both mc-Si and Cz (mono-crystalline) Si wafers were studied with a hyperspectral camera. The samples were studied at room temperature and at 110 K. Only the BB-PL was observed at room temperature. At 110 K, sub-bandgap radiation peaks were clearly identified in the mc-Si wafer but not in the Cz wafer. The sub-bandgap peaks were related to so-called D-band emission lines previously described in the literature [10]. Whereas previous studies [14, 22, 77, 78], were only based on point measurements, the hyperspectral images yielded images of the spatial distribution of the D-band emissions. These images made it possible to study the correlation between the four D-lines, spatially and not only point by point. The measurements support the theory that the D1/D2 pair has a different origin than the D3/D4 pair. Moreover, variations in the intensity ratio between D1 and D2 indicates that D1 and D2 do not always appear together. The same was shown for D3 and D4, and D3 in particular had some very intense spots. An additional emission at 0.75 eV was also observed. This paper showing images of D-band emissions of a whole wafer.

Paper III: Characterization of silicon wafers for photovoltaic applications using hyperspectral imaging

In this article the goal was to further improve the analysis of the hyperspectral images by using multivariate statistics to extract the information from the data cube and by using image alignment to visualize the comparison of hyperspectral images and images obtained by an independent technology. MCR was chosen as a statistical method to extract the interesting signals from the hyperspectral images. There was a good agreement between the score images and the manually extracted D-band images in the studied wafers. The MCR also revealed a new or little described emission at 0.75 eV. Additionally, the high intensity signal with emission near D3, as found in Paper II, was identified as a separate signal called VID3. A calibrated CDI image was obtained to validate the BB results from the hyperspectral camera. The validation showed good agreement between the hyperspectral BB image and the CDI image although the hyperspectral image had better contrast. The differences in contrast made the alignment of the images difficult since similar features must be identified in both images. Different approaches for image alignment were tested. The chosen method was to create a contrast image of the hyperspectral image by summing up the signals from selected wavelengths to be used for input for the alignment procedure. A procedure to locate the corners by finding

the crossing point of the edges was implemented in a software package called Scorpion. The coordinates of the corners were extracted for use in an affine transform of all the channels in Matlab.

Paper IV: Distribution of radiative crystal imperfections through a silicon ingot

The hyperspectral technology has been applied on a larger dataset in this paper, where defect related luminescence has been visualized throughout an entire silicon block. A set of 50 wafers evenly distributed through a silicon block were measured with the hyperspectral camera at room temperature and cooled to 80 K. The wafers were also imaged with a regular photographic camera and with MW-PCD. The latter is a technique to map the interstitial iron content. All the different images of the 50 wafers were aligned to a common coordinate system using the technique described in Chapter 2.4.2. It was a comprehensive task since the contrasts in the hyperspectral images vary with the height of the block and edges were not well defined. The data for each D-line, BB-PL and regular photograph across the full height of the silicon block were extracted as a 3D model. The 3D models were imported to Python Mayavi for visualization. This made it possible to not only see the defects for one wafer but for all the wafers in the stack simultaneously. This made it possible to map how the different radiative emissions were distributed through a silicon ingot. This study also confirmed and visualized the presence of the signal called VID3. Advanced imaging techniques were shown for visualization of defects overlaid a standard RGB image and overlaid a PL image as shown in Paper IV for single wafers.

Chapter 4

Conclusion and further work

The first goal of this thesis was to clarify if it was at all possible to detect emissions from sub band gap by using hyperspectral imaging techniques. Analysis of the hyperspectral images of silicon wafers showed clear sub bandgap signals. The intensity as well as the spatial location of the emitted signal could be identified. Hyperspectral photoluminescence was therefore a suitable method for studying silicon wafers.

The second goal was to develop a method using hyperspectral imaging to characterize wafers. This required testing of excitation sources, wafer cooling methods as well as image processing and analysis methods. The system developed in this thesis proved to be highly sensitive, able to detect weak defect related luminescent signals. The method is fast, non-contact and non-destructive requiring no sample preparation.

The hyperspectral imaging method was then applied to commercial wafers to get a better understanding of the radiative defects. The 3D-visualization of a stack of hyperspectral images made it possible to see the distribution of radiative signals through a silicon ingot. The method developed for image alignment can be used to compare measurements from hyperspectral imaging with other characterization measurements. This work has revealed new knowledge of the spatial distribution and presence of the different D-bands. In particular, the D1 and D2 bands do not always coexist and based on our results cannot be regarded as a pair. The presence of the D3 and D4 band are more likely a pair, assuming that the emission VID3 is a separate signal. By using multivariate statistics, VID3 was extracted as a separate signal of point defects. The signal of 0.75 eV was shown to be distributed as point defects in the wafers.

In future studies, comparisons of hyperspectral imaging with several complementary measurements should be conducted in order to improve the understanding of the physics behind the emissions. Several projects have been initiated to study the correspondence

between the defect related luminescence and other scanning or image based complementary methods. One recently initiated project aiming to improve the understanding of the different emission peaks compares our hyperspectral imaging method and defect classification obtained by EL and reverse EL. In another ongoing study, different defect related emissions against grain boundaries and grain orientation on a large dataset of commercial full sized wafers is investigated. A full temperature study, characterizing the radiative peaks in the temperature range 100-300 K, will provide more information on the temperature dependence of the different peaks. Furthermore, the hyperspectral imaging method should be developed further by deriving a calibration method for the setup, to be able to compare the intensity in images obtained in different experimental setups.

Bibliography

[1] G Masson, M Latour, M Rekinger, T Theologitis, and M Papoutsi. Global Market Outlook for Photovoltaics 2013-2017. Technical report, January 2013.

[2] G Coletti, P Bronsveld, G Hahn, W Warta, D MacDonald, B Ceccaroli, K Wambach, N Le Quang, and J M Fernandez. Impact of Metal Contamination in Silicon Solar Cells. *Advanced Functional Materials*, 21(5):879–890, February 2011.

[3] E J Øvrelid and E Olsen. Impurities in solar grade silicon and their effect on solar cell performance. Technical Report STF24 A04810, Sintef Material and Chemistry, Norway, 2004.

[4] M. A Green. *Solar cells*. Operating principles, technology and system applications. The University of New South Wales, 1998.

[5] R Abbaschian, L Abbaschian, and R E Reed-Hill. *Physical Metallurgy Principles*. Cengage Learning, Stamford, fourth edition, March 2009.

[6] D Hull and D J Bacon. *Introduction to Dislocations*. Elsevier, fifth edition, March 2011.

[7] G Coletti, D MacDonald, and D Yang. Role of Impurities in Solar Silicon. In *Advanced Silicon Materials for Photovoltaic Applications*, pages 79–125. John Wiley & Sons, Ltd, Chichester, UK, June 2012.

[8] B Sopori. Impurities and defects in photovoltaic Si devices: A review. In V Kumar and S K Agarwal, editors, *10th International Workshop on the Physics of Semiconductor Devices*, pages 1214–1226. SPIE-Int Soc. Optical Engineering, 2000.

[9] K Graff. *Metal Impurities in Silicon-Device Fabrication*. Springer-Verlag, second edition, March 1999.

[10] N A Drozdow, A A Patrin, and V D Tkachev. Recombination radiation on dislocations in silicon. *Pis'ma Zh. Exsp. Teor. Fiz*, 23(597), June 1976.

[11] S Rein. *Lifetime Spectroscopy: A Method of Defect Characterization in Silicon for Photovoltaic Applications* . Springer-Verlag, June 2005.

[12] T Arguirov. *Electro-optical properties of dislocations in silicon and their possible application for light emitters*. PhD thesis, der Brandenburgischen Technischen Universität Cottbus, Cottbus, Germany, 2007.

[13] T Arguirov, W Seifert, M Kittler, and J Reif. Temperature behaviour of extended defects in solar grade silicon investigated by photoluminescence and EBIC . *Materials Science and Engineering*, B102, May 2003.

[14] M Tajima, Y Iwata, F Okayama, H Toyota, H Onodera, and T Sekiguchi. Deep-level photoluminescence due to dislocations and oxygen precipitates in multicrystalline Si. *Journal of Applied Physics*, 111(11):113523–113523, 2012.

[15] W Piper and F Williams. Theory of Electroluminescence. *Physical Review*, 98(6):1809–1813, June 1955.

[16] T Gfroerer. Photoluminescence in Analysis of surfaces and interfaces. In R Meyers, editor, *Encyclopedia of Analytical Chemistry*, pages 9209–9231. John Wiley & Sons Ltd, Chichester, 2000.

[17] Feng Li, ZhongQuan Ma, XiaJie Meng, Peng Lü, ZhengShan Yu, and Bo He. Influence of surface passivation on the minority carrier lifetime, Fe-B pair density and recombination center concentration. *Chinese Science Bulletin*, 55(17):1828–1833, June 2010.

[18] T Mchedlidze, W Seifert, M Kittler, A T Blumenau, B Birkmann, T Mono, and M Müller. Capability of photoluminescence for characterization of multi-crystalline silicon. *Journal of Applied Physics*, 111(7):073504, 2012.

[19] M. A Green and M J Keevers. Optical-Properties of Intrinsic Silicon at 300 K. *Progress in Photovoltaics*, 3(3):189–192, 1995.

[20] R Sauer, J Weber, J Stolz, E R Weber, K Küsters, and H Alexander. Dislocation-related photoluminescence in silicon. *Appied Physics A Solids and Surfaces*, July 1984.

[21] V Higgs, M Goulding, A Brinklow, and P Kightley. Characterization of epitaxial and oxidation-induced stacking faults in silicon: The influence of transition-metal contamination. *Appl.Phys Lett*, 60(11):1369–1371, 1992.

[22] S Ostapenko, I Tarasov, J P Kalejs, C Haessler, and E-U Reisner. Defect monitoring using scanning photoluminescence spectroscopy in multicrystalline silicon wafers. *Semiconductor Science and Technology*, 15(8):840–848, June 2000.

[23] T Sekiguchi and K Sumino. Cathodoluminescence study on dislocations in silicon. *Journal of Applied Physics*, 79(6):3253, 1996.

[24] S Pizzini, M Guzzi, E Grilli, and G Borionetti. The photoluminescence emission in the 0.7-0.9 eV range from oxygen precipitates, thermal donors and dislocations in silicon. *J. Phys.: Condens. Matter*, 12(49):10131–10143, November 2000.

[25] T Mchedlidze, T Arguirov, O Kononchuk, M Trushin, and M Kittler. Structures responibie for radiative and non-radiative recombinations activity of dislocations in silicon. *Phys. Status Solidi*, 8(3):991–995, 2011.

[26] T G Brown. Optical emission at 1.32um from sulfur-doped crystalline silicon. *Appl.Phys Lett*, 49(5):245–247, August 1986.

[27] C Krause, D Mankovics, H Krause, T Arguirov, and M Kittler. On the origin of intense luminescence at 0.93 eV from multi-crystalline silicon. *Journal of Applied Physics*, 114(3):034902, 2013.

[28] K Lauer, A Laades, H Übensee, H Metzner, and A Lawerenz. Detailed analysis of the microwave-detected photoconductance decay in crystalline silicon. *Journal of Applied Physics*, 104(10):104503, 2008.

[29] D V Lang. Deep-level transient spectroscopy: A new method to characterize traps in semiconductors. *Journal of Applied Physics*, 45(7):3023, 1974.

[30] M Schubert, J Schön, P Gundel, H Habenicht, W Kwapil, and W Warta. Imaging of Metal Impurities in Silicon by Luminescence Spectroscopy and Synchrotron Techniques. *Journal of Electronic Materials*, 39(6):787–793, March 2010.

[31] M Di Sabatino, A Dons, J Hinrichs, and L Arnberg. Determination of relative sensitivity factors for trace element analysis of solar cell silicon by fast-flow glow discharge mass spectrometry. *Spectrochimica Acta Part B-Atomic Spectroscopy*, 66 (2):144–148, February 2011.

[32] M Di Sabatino. Detection limits for glow discharge mass spectrometry (GDMS) analyses of impurities in solar cell silicon. *Measurement*, 50:135–140, April 2014.

[33] V Higgs and M Kittler. Investigation of the recombination activity of misfit dislocations in Si/SiGe epilayers by cathodoluminescence imaging and the electron beam induced current technique. *Applied Physics Letters*, 63(15):2085–2087, 1993.

[34] T Buonassisi, A Istratov, M Heuer, M Marcus, R Jonczyk, J Isenberg, B Lai, Z Cai, S Heald, W Warta, R Schindler, G Willeke, and E Weber. Synchrotron-based investigations of the nature and impact of iron contamination in multicrystalline silicon solar cells. *Journal of Applied Physics*, 97(7):074901, 2005.

[35] S Binetti, J Libal, M Acciarri, M Di Sabatino, H Nordmark, E J Øvrelid, J C Walmsley, and R Holmestad. Study of defects and impurities in multicrystalline silicon

grown from metallurgical silicon feedstock. *Materials Science and Engineering: B*, 159-160:274–277, March 2009.

[36] T Trupke, R. A Bardos, M. C Schubert, and W Warta. Photoluminescence imaging of silicon wafers. *Applied Physics Letters*, 89(4):044107–044107, 2006.

[37] T Trupke, B Mitchell, J W Weber, W McMillan, R. A Bardos, and R Kroeze. Photoluminescence Imaging for Photovoltaic Applications. *Energy Procedia*, 15: 135–146, January 2012.

[38] T Trupke, J Nyhus, and J Haunschild. Luminescence imaging for inline characterisation in silicon photovoltaics. *physica status solidi (RRL) - Rapid Research Letters*, 5(4):131–137, February 2011.

[39] T Trupke, R. A Bardos, and M. D Abbott. Self-consistent calibration of photoluminescence and photoconductance lifetime measurements. *Applied Physics Letters*, 87(18):184102–184102, 2005.

[40] S Herlufsen, J Schmidt, D Hinken, K Bothe, and R Brendel. Photoconductance-calibrated photoluminescence lifetime imaging of crystalline silicon. *physica status solidi (RRL) - Rapid Research Letters*, 2(6):245–247, December 2008.

[41] J Giesecke, M Schubert, B. Michl, F. Schindler, and W Warta. Minority carrier lifetime imaging of silicon wafers calibrated by quasi-steady-state photoluminescence. *Solar Energy Materials and Solar Cells*, 95(3):1011–1018, December 2011.

[42] D MacDonald, J Tan, and T Trupke. Imaging interstitial iron concentrations in boron-doped crystalline silicon using photoluminescence. *Journal of Applied Physics*, 103(7):073710, 2008.

[43] M. C Schubert, H Habenicht, and W Warta. Imaging of Metastable Defects in Silicon. *Photovoltaics, IEEE Journal of*, 1(2):168–173, 2011.

[44] M Bail, J Kentsch, R Brendel, and M Schulz. Lifetime mapping of Si wafers by an infrared camera [for solar cell production]. In *28th IEEE Photovoltaic Specialists Conference*, pages 99–103. IEEE, 2000.

[45] D Mankovics, A Klossek, Ch Krause, T Arguirov, W Seifert, and M Kittler. Luminescence of defects and breakdown sites in mulicrystalline silicon solar cells. *Phys. Status Solidi*, A 209(10):1908–1912, 2012.

[46] Trupke et al. Progress with luminescence imaging for the characterisation of silicon wafers and solar cells. In *Proceedings 22nd European Photovoltaic Solar Energy Conference (22nd EU PVSEC)*, pages 22–31, January 2007.

[47] R P Schmid, D Mankovics, T Arguirov, M Ratzke, T Mchedlidze, and M Kittler. Rapid dislocation-related D1-photoluminescence imaging of multicrystalline Si wafers at room temperature. *physica status solidi (a)*, 208(4):888–892, January 2011.

[48] F Yan, S Johnston, M Al-Jassim, K Zaunbrecher, O Sidelkheir, and A Blosse. Defect-Band Emission Photoluminescence Imaging on Multi-Crystalline Si Solar Cells. In *37 IEEE Photovoltaic Specialists conference*, May 2011.

[49] D Mankovics, R Schmid, T Arguirov, and M Kittler. Dislocation-related photoluminescence imaging of mc-Si wafers at room temperature. *Cryst. Res. Technol.*, 47 (11):1148–1152, 2012.

[50] M Peloso, J Sern Lew, T Trupke, M Peters, R Utama, and A Aberle. Evaluating the electrical properties of silicon wafer solar cells using hyperspectral imaging of luminescence. *Applied Physics Letters*, 99(22):221915, 2011.

[51] M Peloso, J Lew, B Hoex, and A Aberle. Line-Imaging Spectroscopy for Characterisation of Silicon Wafer Solar Cells. *Energy Procedia*, 15:171–178, January 2012.

[52] Q Li, W Wang, C Ma, and Z Zhu. Detection of physical defects in solar cells by hyperspectral imaging technology. *Optics & Laser Technology*, 42(6):1010–1013, September 2010.

[53] A Delamarre. *Development of luminescence based characterisation methos for solar cells.* PhD thesis, Sorbonne University, October 2013.

[54] H Grahn and P Geladi. *Techniques and applications of hyperspectral image analysis.* John Wiley & Sons Ltd, 2007.

[55] J Lerner, N Gat, and E Wachman. *Approaches to Spectral Imaging Hardware.* John Wiley & Sons, Inc., Hoboken, NJ, USA, May 2001.

[56] A Delamarre, L Lombez, and J Guillemoles. Contactless mapping of saturation currents of solar cells by photoluminescence. *Applied Physics Letters*, 100(13): 131108, 2012.

[57] R Gonzales and R Woods. *Digital image processing.* Pearson, third ed. edition, 2008.

[58] G Wolberg and S Zokai. Robust image registration using log-polar transform. In *2000 international conferenceon image processing*, pages 493–496. IEEE, 2000.

[59] D Lowe. Distinctive Image Features from Scale-Invariant Keypoints. *International Journal of Computer Vision*, 60(2):91–110, January 2004.

[60] Scorpion Vision 9, Tordivel AS, Oslo, Norway. 2012. URL http://www.tordivel.no.

[61] MATLAB release 2013a, The Mathworks Inc., USA. 2013.

[62] Enthought Python 2.7. 2013. URL www.enthought.com.

[63] P Ramachandran and G Varoquaux. Mayavi2, 2013. URL http://code.enthought.com/projects/mayavi.

[64] S Wold, K Esbensen, and P Geladi. Principal component analysis. *Chemometrics and Intelligent Laboratory Systems*, 2(1-3):37–52, August 1987.

[65] P Comon. Independent Component Analysis. *Higher Order Statistics*, January 1992.

[66] R Tauler, B Kowalski, and S Fleming. Multivariate curve resolution applied to spectral data from multiple runs of an industrial process. *Analytical Chemistry*, 65 (15):2040–2047, August 1993.

[67] X Zhang and R Tauler. Application of Multivariate Curve Resolution Alternating Least Squares (MCR-ALS) to remote sensing hyperspectral imaging. *Analytica Chimica Acta*, 762:25–38, January 2013.

[68] A A Gowen, C P O'Donnell, M Taghizadeh, P J Cullen, J M Frias, and G Downey. Hyperspectral imaging combined with principal component analysis for bruise damage detection on white mushrooms (Agaricus bisporus). *Journal of Chemometrics*, 22(3-4):259–267, 2008.

[69] J Xing, W Saeys, and J De Baerdemaeker. Combination of chemometric tools and image processing for bruise detection on apples. *Computers and Electronics in Agriculture*, 56(1):1–13, March 2007.

[70] C Ruckebusch and L Blanchet. Multivariate curve resolution: A review of advanced and tailored applications and challenges. *Analytica Chimica Acta*, 765:28–36, February 2013.

[71] PLS Toolbox 7.03, Eigenvector Research, Wennatcheee, US. 2013.

[72] R Bro and S De Jong. A fast non-negativity-constrained least squares algorithm. *Journal of Chemometrics*, 11(5):393–401, September 1997.

[73] R Tauler, A Smilde, and B Kowalski. Selectivity, local rank, three-way data analysis and ambiguity in multivariate curve resolution. *Journal of Chemometrics*, 9(1):31–58, January 1995.

[74] A Juan, R Tauler, R Dyson, C Marcolli, M Rault, and M Maeder. Spectroscopic imaging and chemometrics: a powerful combination for global and local sample analysis. *TrAC Trends in Analytical Chemistry*, 23(1):70–79, January 2004.

[75] N Gallagher, J Shaver, E Martin, J Morris, B Wise, and W Windig. Curve resolution for multivariate images with applications to TOF-SIMS and Raman. *Chemometrics and Intelligent Laboratory Systems*, 73(1):105–117, September 2004.

[76] Y Koshka, S Ostapenko, I Tarasov, S McHugo, and J P Kalejs. Scanning room-temperature photoluminescence in polycrystalline silicon. *Applied Physics Letters*, 74(11):1555, 1999.

[77] A V Mudryi, A I Patuk, I A Shakin, A G Ulyashin, R Job, W R Fahrner, A Fedotov, A Mazanik, and N Drozdov. Impurities and defects in multicrystalline silicon for solar cells: low-temperature photoluminescence investigations. *Solar Energy Materials and Solar Cells*, 72(1-4):503–508, April 2002.

[78] M Inoue, H Sugimoto, M Tajima, Y Ohshita, and A Ogura. Microscopic and spectroscopic mapping of dislocation-related photoluminescence in multicrystalline silicon wafers. *Journal of Materials Science: Materials in Electronics*, 19(S1):132–134, February 2008.

[79] E Olsen, A S Flø, and I Burud. Radiative Inter Band GAP Recombination in Unpassivated AS-Cut Multicrystalline Silicon Wafers. *28th European Photovoltaic Solar Energy Conference and Exhibition*, pages 1400–1402, 2013.

Paper 1

Spectral and spatially resolved imaging of photoluminescence in multicrystalline silicon wafers

E. Olsen[a)] and A.S. Flø

Department of Mathematical Sciences and Technology, Norwegian University of Life Sciences, Drøbakveien 31, N-1432 Ås, Norway

The photoluminescent properties of multicrystalline silicon wafers have been studied using hyperspectral imaging in the region 900–1700 nm. Hyperspectral imaging provides high resolution macroscopic images in both the spatial and spectral dimensions over a time frame of seconds. Energy states introduced in the bandgap of Si from crystal imperfections resulted in increased recombination of photogenerated free charge carriers. Spectral resolution in the near infrared enabled us to spatially image specific radiative recombination processes through traps in the Si bandgap. Hyperspectral imaging is a fast, non-contact, and non-destructive method, giving it potential for industrial applications. © *2011 American Institute of Physics*. [doi:10.1063/1.3607307]

Luminescence imaging of multicrystalline silicon (mc-Si) wafers for solar cell applications has been shown to be a powerful method for studying a wide range of parameters affecting solar cell performance.[1–4] Of these, the lifetime and diffusion lengths of minority charge carriers in wafers,[2] shunting,[5,6] series resistance,[7] and crystal imperfections[8,9] are of particular interest. Visualizing these parameters as images has become a valuable tool for the photovoltaic (PV) industry in the task of optimizing process parameters to achieve ever higher solar cell efficiencies.

Hyperspectral imaging is a well documented method where a spectrally as well as spatially resolved image is recorded. The setup relies on a charge coupled device (CCD) camera focusing on a line rather than the entire sample. The line signal is resolved spectrally by directing it through a diffracting slit at the focal point of the entrance optics before the collimating lenses. The spectrally resolved signal is then recorded by the CCD chip, effectively sacrificing one dimension of spatial resolution. This dimension is then regained by physically moving (scanning) either the camera or the sample at a specified rate. The method has been used for studying physical defects such as cracks and surface contamination in processed solar cells.[10]

Recombination of photogenerated charge carriers through states in the bandgap may be of radiative nature and result in the emittance of photons at higher wavelengths (lower energy) than the Si band to band (Si-BB) transition. Such energy states within the Si bandgap may be introduced by structural crystal defects and impurities. Such states have been extensively studied and mapped.[1] However, due to the extremely low densites of these states, the emitted signals will be very weak compared to the primary photoluminescence (PL) signal.

In this Letter, we demonstrate that hyperspectral imaging can be used to characterize surface passivated, boron doped, multicrystalline silicon wafers without a pn-junction. We employ an InGaAs-based camera with a spectral range from 900 nm to 1700 nm and a spectral resolution of 5 nm.

This enables us to specifically extract the signal caused by luminescence due to radiative recombination over the bandgap of silicon at 1150 nm. We further demonstrate the potential for imaging individual crystal imperfections associated with radiative recombination through energy states introduced into the Si bandgap. The recording time of the images is on the order of seconds.

Conventional p-doped (boron, 1.0 $\Omega\cdot$cm, 240 μm thickness) multicrystalline silicon wafers with dimensions 50×50 mm were used in this study. The wafers were surface passivated by amorphous Si (a-Si:H). Band-to-band (BB) photoluminescence was studied at room temperature (RT) by placing the wafer on a polished stainless steel surface. The sample was cooled to 120 K on a liquid nitrogen cooled surface of polished aluminium. The excitation source was a 808 nm/2 W laser diode with a line generating lens. The photon flux at the sample was on the order of 4.0×10^{18} cm^{-2} (20 suns). The practical spatial resolution of the system (Norsk Elektrooptikk SWIR 320i) was on the order of 330 μm. The signal from the sample was filtered by a 850 nm low-pass optical filter before entering the focusing optics. The contrast and brightness of the images were adjusted for optimal printed visibility with the image software GIMP 2.6.

Photoluminescence from the Si band-to-band transition with a center wavelength of 1150 nm was recorded by the hyperspectral camera and is presented as a spatially resolved image in Figure 1(a). Strong PL signals giving images with good quality were recorded, albeit somewhat limited by the spatial resolution of the system. Physical features of the wafer such as grain boundaries are depicted with good contrast. Sub-grain boundaries are also evident as are larger regions with decreased PL activity. Uneven brightness in the image was caused by uneven illumination by the solid state laser diode.

The spectrum of a high intensity luminescent region in the wafer at room temperature (RT, 300 K) (marked 1 in Figure 1(a)) is shown in Figure 2. It exhibits a strong signal centered at 1150 nm attributed to the band-to-band PL of Si, as expected. No apparent signals were recorded in the higher wavelength region corresponding to recombination through radiative active states in the bandgap at RT. A shoulder-like

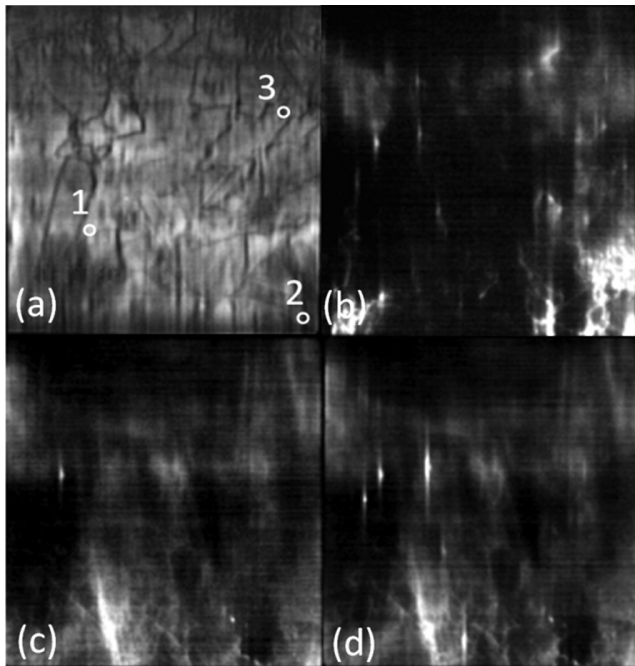a)Author to whom correspondence should be addressed. Electronic mail: espen.olsen@umb.no.

FIG. 1. (a) Intensity image of the band-to-band photoluminescense signal from the multicrystalline silicon wafer sample with center frequency 1150 nm/1.09 eV at 300 K. The image was generated by integrating the signals between 1100 and 1200 nm. (b) Intensity image of the signal with center frequency 1520 nm/0.816 eV at 120 K. (c) Intensity image of the signal with center frequency 1270 nm/0.977 eV at 120 K. (d) Intensity image of the signal with center frequency 1320 nm/0.940 eV at 120 K.

feature was recorded at the lower energy side of the peak (1200-1250 nm). This was due to indirect bandgap transitions of the excited minority charge carriers involving interactions with more than one phonon.

The wafer was cooled to 120 K as described above in order to increase the signal from luminescent active states. A wide range of signals in the range 1200–1700 nm were recorded at lower temperatures as energy transitions became
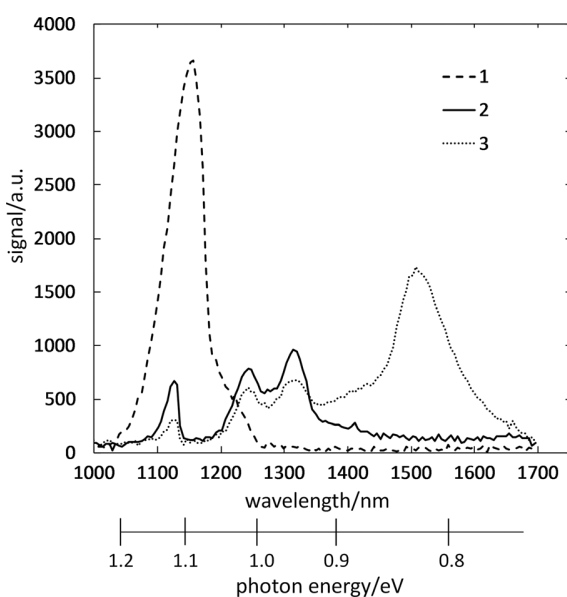

FIG. 2. The recorded spectra from the areas marked 1 (300 K), 2 and 3 (120 K) in Figure 1(a), respectively.

radiative. The characteristics of these varied from spectrally sharp peaks and highly localized signals to spatially distributed and spectrally broader peaks. Metallic impurities as Mo, Ni, or Fe and intermetallic particle clusters such as Cu_3Si have a tendency to accumulate at localized positions in the grain boundaries in mc-Si.[11–14] Dislocations may be pinned to grain boundaries in large numbers or they may be distributed more evenly within certain grains.

In this Letter, we discuss briefly two inter-bandgap spectral signals, one signal with a center wavelength of 1520 nm/0.816 eV and a signal consisiting of two peaks in the range 1250–1350 nm. These peaks were seemingly coupled by some physical mechanism as they frequently appeared together as a characteristic double peak with center wavelengths 1270 nm/0.977 eV and 1320 nm/0.940 eV. A number of other spectral features were recorded in the images, to be the subject of further studies.

The spectrum from the area marked 2 in Figure 1(a) is shown in Figure 2. It is characterized by a strong, main signal with a center wavelength of 1520 nm/0.816 eV. Additionally, two characteristic peaks at 1270 nm/0.977 eV and 1320 nm/0.940 eV are present at lower intensities. The BB PL signal from Si was quenched to a large extent, but a remnant is evident at a significantly smaller intensity than the signals caused by recombination through inter-bandgap states. The signal at 1520 nm/0.816 eV is depicted as a spatially resolved image in Figure 1(b) and seems to associate primarily with two larger, distributed areas in the bottom left and right part of the wafer. These areas also exhibit low lifetime of minority charge carriers evident from the low intensity in the BB PL image in Figure 1(a). More shadowy contrast was recorded in other parts of the wafer at this wavelength. The distributed nature over certain, specific areas suggests an origin related to dislocations. This statement is, however, of speculative nature and calls for further investigations by dislocation mapping techniques. Studies of the iron-boron complex FeB have shown interstitially positioned iron (Fe_i), which readily forms the FeB complex in boron doped Si, to appear with a distributed nature in mc-Si in heavily contaminated samples.[1] Assuming a one step recombination process and a Si bandgap of 1.15 eV at 120 K, the signal with energy 0.816 eV (1520 nm) may be attributed to a defect level either at E_t-E_v or E_c-E_t = 0.334 eV. The recombination active acceptor state introduced by FeB has been extensively studied and is on average reported at E_c-E_t = 0.26 ± 0.03 eV.[12] This is not in accordance with the mechanism reported here. However, a radiative dislocation state emitting at 0.8 eV has been reported.[13] This is close to the value found in this study.

Figure 2 shows the spectral response from the area marked 3 in Figure 1(a). Apart from a partially quenched Si BB PL peak at 1150 nm, two sharp peaks are seen in the spectrum. Their center wavelengths are 1270 nm/0.977 eV and 1320 nm/0.940 eV, respectively. These two peaks are in general found in most spectra from low-lifetime regions of the wafer. The signal from the peak at 1270 nm/0.977 eV is shown as a spatially resolved image in Figure 1(c) and the peak at 1320 nm/0.940 eV is shown in Figure 1(d). The images show that these signals exhibit both distributed and sharp, localized characteristics.

The distributed signals in Figures 1(c) and 1(d) seem to be correlated since the images show the same features. By comparing the image of the Si BB PL signal (Figure 1(a)) and the peak imaged (Figs. 1(c) and 1(d)), it is evident that there is a negative correlation between the Si BB PL and these since low luminosity parts of the PL image show higher signal strength from the peaks. This is as expected and suggests that the physical mechanisms associated with these signals are connected to lower lifetimes of minority charge carriers, i.e., enhanced recombination.

Striking features of the images depicted in Figures 1(c) and 1(d) are the sharp, localized signals evident as individual point-like areas with high luminosity. In some of these areas, the signals at 1270 nm/0.977 eV and 1320 nm/0.940 eV appear together and in other areas they do not. Comparing the images in Figures 1(c) and 1(d) to the Si BB PL image in Figure 1(a), it is evident that all these areas also have low luminosity in the Si BB PL image. The point-like signals are distorted in one dimension along the excitation laser line. This may be due to back-reflection from the sample holder with subsequent scattering from the impurity. Metallic impurities either in the form of precipitated silicides or as individual metallic inclusions have been reported in transmission electron microscope (TEM) studies.[14] These tend to precipitate at grain boundaries and triple points in the multicrystalline material. They are often associated with dislocation loops or networks.

The photoluminescent properties of mc-Si wafers in the range 900 to 1700 nm have been studied by hyperspectral imaging. The PL from the band-to-band transition in Si may be used for generating images with contrast related to the lifetime of excited minority charge carriers. Furthermore, the method enables signals originating from recombination through states in the bandgap of Si to be extracted. These signals may be used for imaging the distribution of crystal defects such as contaminating elements and dislocations associated with known energy states in the bandgap.

[1] M. C. Schubert, J. Schön, P. Gundel, H. Habenicht, W. Kwapil, and W. Warta, J. Electron. Mater. **39**, 6 (2010).

[2] T. Trupke, R. A. Bardos, M. C. Schubert, and W. Warta, Appl. Phys. Lett. **89**, 044107 (2006).

[3] T. Trupke, E. Pink, R. A. Bardos, and M. D. Abbott, Appl. Phys. Lett. **90**, 093506 (2007).

[4] T. Arguirov, W. Seifer, G. Jia, and M. Kittler, Semiconductors **41**, 4 (2007).

[5] M. Kasemann, D. Grote, B. Walter, W. Kwapil, T. Trupke, Y. Augarten, R. A. Bardos, E. Pink, M. D. Abbott, and W. Warta, Prog. Photovoltaics **16**, 297 (2008).

[6] O. Breitenstein, J. Bauer, T. Trupke, and R. A. Bardos, Prog. Photovoltaics **16**, 325 (2008).

[7] H. Kampwerth, T. Trupke, W. Weber, and Y. Augarten, Appl. Phys. Lett. **93**, 202102 (2008).

[8] D. MacDonald, J. Tan, and T. Trupke, J. Appl. Phys. **103**, 073710 (2008).

[9] H. Habenicht, M. C. Schubert, and W. Warta, J. Appl. Phys., **108**, 034909 (2010).

[10] Q. Li, W. Wang, C. Ma, and Z. Zhu, Opt. Laser Technol. **42**, 1010 (2010).

[11] K. Graff, *Metal Impurities in Silicon-Device Fabrication* (Springer, Berlin, 1995).

[12] S. Rein, *Lifetime Spectroscopy – A Method of Defect Characterization in Silicon for Photovoltaic Applications* (Springer, Berlin, 2005).

[13] Y. Koshka, S. Ostapenko, I. Tarasov, S. McHugo, and J. P. Kalejs, Appl. Phys. Lett. **74**, 11 (1999).

[14] E. Olsen, H. Nordmark, and E. Øvrelid, in *Proceedings of the 20th European Photovoltaic Solar Energy Conference and Exhibition*, Barcelona, Spain, June 6-10, 2005, p. 1082.

Paper 2

On the origin of inter band gap radiative emission in crystalline silicon

I. Burud, A. S. Flø, and E. Olsen[a]
Norwegian University of Life Sciences, Dept. Mathematical Sciences and Technology, Drøbakveien 31, N-1432 Ås, Norway

Crystal imperfections degrade the quality of multicrystalline silicon wafers by introducing alternative recombination mechanisms. Here we use non-destructive hyperspectral imaging to detect photoluminescence signals from radiatively active recombination processes over the wafer with a highly resolved spectral third dimension. We demonstrate that band-to-band recombination can be visually separated from recombination through traps across the whole surface of a wafer using hyperspectral imaging. Our samples are studied in the near infrared wavelength region, 900-1700 nm, which includes the region of the so called D-band emission lines. These constitute four resolved emission lines found in the photoluminescence spectrum of silicon, commonly related to recombination through shallow inter-band gap energy levels near the conduction- and valence band edges. The shape and structure of these emissions from our measurements suggest that all the D-lines have different origins. *Copyright 2012 Author(s). This article is distributed under a Creative Commons Attribution 3.0 Unported License.* [http://dx.doi.org/10.1063/1.4766588]

I. INTRODUCTION

Multicrystalline silicon (mc-Si) used in photovoltaic applications contains various amounts of crystal imperfections, such as point defects, grain boundaries and dislocations, limiting the efficiency of solar cells through increased recombination of photogenerated charge carriers.[1] Understanding the origin of various types of crystal imperfections, as well as their influence on the recombination routes in the crystal, is crucial in the aim of improving the solar cell process. Often, imperfections are grouped in clusters since impurities in mc-Si tend to segregate in the strain field around dislocations in the crystal. This is particularly true for transition metal impurities introduced during processing of the silicon wafer. In a detailed study of dislocations and metal silicides in crystalline silicon, performed by Seibt *et al.*[2] it was found that electron-hole-pair recombination at a dislocation site mainly runs via its shallow levels and is strongly increased by impurities bound to the dislocation core. It has also been suggested that removal or deactivation of recombination active impurities from structural defects such as dislocations by gettering, eliminates deep-level recombination routes, but does not influence the shallow levels.[3] It is therefore particularly important to understand the origin of the shallow band recombination routes.

Spectra from the near infrared region (NIR) of cooled mc-Si crystals often contain 4 pronounced emission lines, called D-band emission lines. The 4 lines denoted by D1 - D4 have central peaks located at 0.812, 0.875, 0.934 and 1.00 eV respectively.[4] The D-band lines are generally considered to be related to defects causing recombination through radiatively active, relatively shallow bands, observable in the NIR region.[3,4] During the last decade, much research effort has been invested into understanding the origins of the D-band emission lines, in particular their relation to various types of dislocations and metal contamination.[5] It has been suggested that D1 and D2 lines originate from the

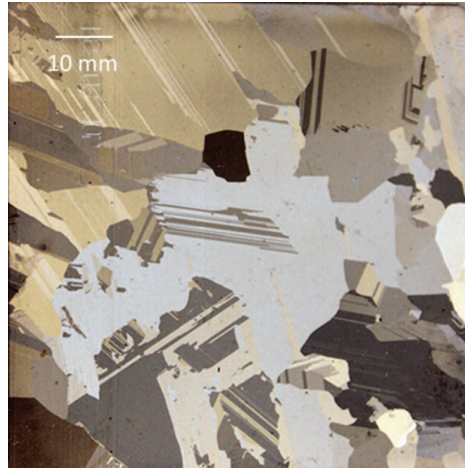---

[a]Electronic mail: espen.olsen@umb.no

FIG. 1. Regular photo of the mc-Si wafer.

defects produced by the same dislocation processes, and likewise for D3 and D4 lines. The former and the latter defects are, however, believed to be different from each other in nature.[4]

   Photoluminescence (PL) imaging of silicon wafers is a powerful non-destructive method to study and characterize crystalline silicon wafers.[6,7] The PL signal being directly related to the minority carrier lifetimes, PL imaging can even be used to map the lifetime across the wafer, as demonstrated by References [8] and [9]. Traditional PL images do not contain any wavelength information and spectroscopy needs to be performed on selected areas of the wafer to obtain this additional information. However, recently it was demonstrated in a pilot study how PL imaging with hyperspectral techniques yields, simultaneously, the Si band-to-band (BB) luminescence image as well as images of luminescence from radiatively active crystal imperfections introducing inter band gap energy states in a mc-Si wafer.[10] Hyperspectral imaging is a form of spectroscopy where a spectrum is sampled at each point in the image plane. This results in a highly sensitive three-dimensional (2+1) image, providing both spatial and spectral information of the sample. In the present work the technique of hyperspectral imaging will be used to study the physics and origins of radiatively active recombination routes, including the D-band emission, on our mc-Si wafer.

II. EXPERIMENTAL SETUP

   The hyperspectral camera used in the study (Norsk Elektrooptikk SWIR 320i) has an InGaAs detector and the spectral range is from 900 nm to 1700 nm. The spatial resolution is on the order of 300 μm with the present set up, and a spectral resolution of 5 nm. A laser (Lasiris Magnum II, 808 nm) with irradiated power density of 2 W/cm^2, corresponding to a photon flux of 8.10^{18} cm^{-2}s^{-1} was employed as excitation source. A 850 nm low-pass optical filter was added to the focusing optics.

   The samples were a p-doped (boron, 1.0 Ω cm, 240 μm thickness) mc-Si wafer with dimension 50 $\times$ 50 mm, and a Cz-Si slug (1 mm thickness). A regular photo of the mc-Si wafer is displayed in Fig. 1. The samples were surface passivated by amorphous Si (a-Si:H) deposited by chemical vapour deposition (CVD). The average lifetime was measured by quasi steady state photoconductance (QSSPC) (Sinton BCT 400) to $25 - 54$ μs for the mc-Si wafer, and to 300-600 μs for the Cz-Si wafer. BB photoluminescence was studied at room temperature (RT) by placing the wafer on a polished stainless steel surface. In order to enhance the signal from luminescent active imperfections, the samples were also cooled to 110 K on a liquid nitrogen cooled surface of polished aluminium.
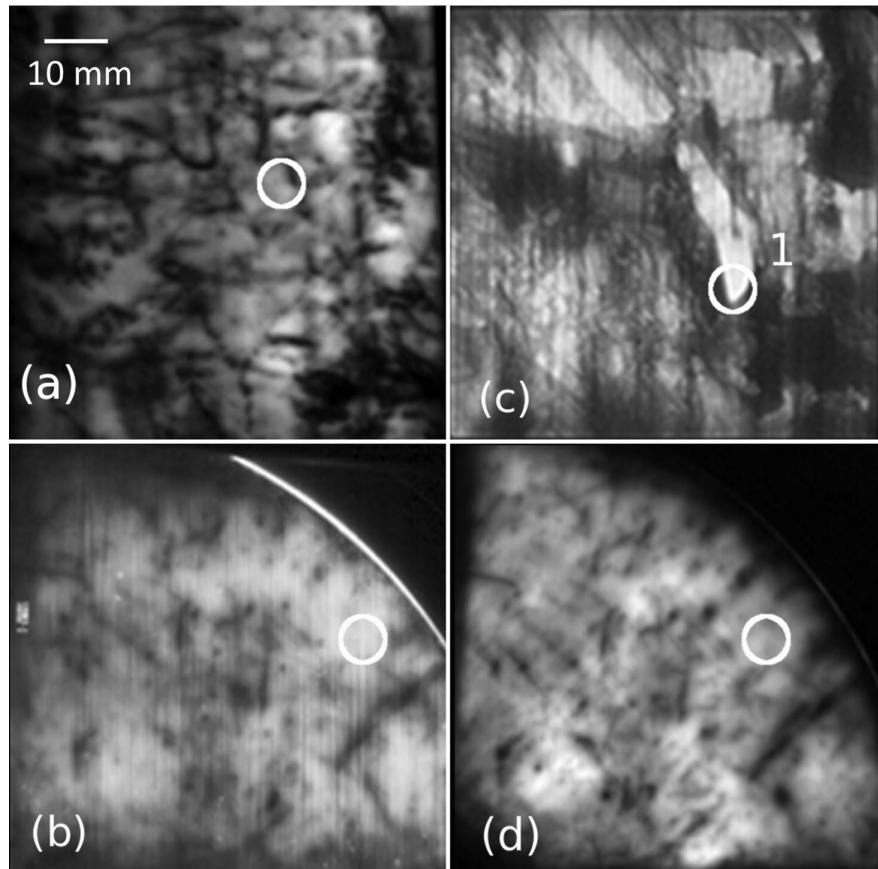
FIG. 2. Intensity images of band-to-band photoluminescence signals from room temperature (300 K) of the mc-Si wafer (a), and the Cz-wafer (b). Band-to-band photoluminescence signal from cooled samples (110 K) of the mc-Si (c) and the Cz-Si wafer (d).

III. EXPERIMENTAL RESULTS

The image file from the hyperspectral camera is composed of a stack of 150 2D-images of the sample, each centered on a specific wavelength in the region 900 – 1700 nm. Such 3D (2+1) image cubes were obtained for both the mc-Si wafer and the Cz-Si wafer, at room temperature (300 K) and at 110 K. Images of the BB photoluminescence at 300 K and 110 K for both wafers are shown in Fig. 2. The grain boundaries are clearly observed as contrasts in the BB mc-Si PL image obtained at 300 K [Fig. 2(a)]. In this image, sub-grain boundaries and point defects are also identified whereas twins are absent. Structure was also seen in BB PL image of the Cz-Si wafer [Fig. 2(b)], similar to the image of the photoluminescence killing centers in Cz wafers reported by Ma *et al.*[11] No other signal other than the Si PL could be detected in our 300 K recordings of the Cz wafer.

The BB photoluminescence images from the cooled Cz and mc-Si wafers are shown in Figs. 2(c) and 2(d) respectively. For the mc-Si wafer, crystallites seen in the regular photo in Fig. 1 are easily recognized. Several signals from radiatively active energy transitions were observed in the cooled mc-Si wafer, and the much studies D-lines described above was clearly identified. A composed colour image showing the D1 (0.82 eV) in red and D2 (0.87 eV) emission in green is shown in Fig. 3(a). Similarly, Fig. 3(b) shows an image of the D3 (0.93 eV) emission in red and D4 (1.0 eV) in green. An additional signal detected at 0.75 eV is shown in Fig. 3(c).

Spectra of selected locations in the wafers are shown in Figure 4. It can be seen that the BB emission from the cooled samples have more narrow spectral peaks than at 300 K, and they are
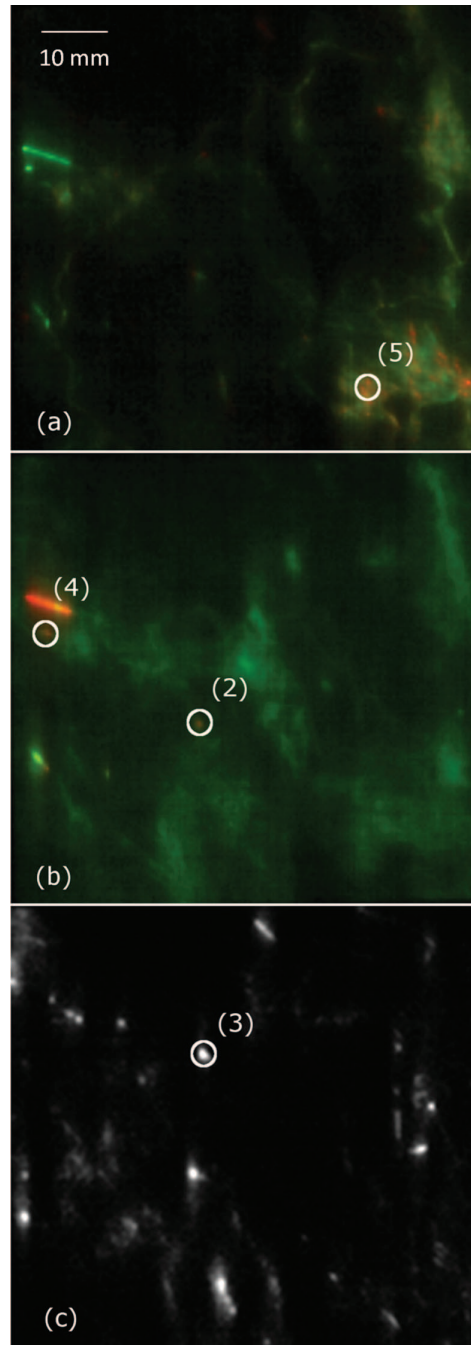
FIG. 3. Composed red and green colour images of the D-band emissions, D1 (0.82 eV) in red and D2 (0.87 eV) in green (a), D3 (0.93 eV) in red and D4 (1.0 eV) in green (b). Image of the 0.75 eV signal (c).

slightly shifted to a higher energy, 1.09 eV compared to 1.08 eV at 300 K [Fig. 4(a)]. A lower energy peak at 1.04 eV was also observed at 110 K, which is generally regarded as the phonon replica of the BB peak. The D-band emission observed in the cooled mc-Si wafer [Figs. 3(a) and 3(b)] also show up in the spectra. The intensity ratios between the various emission lines depend strongly on the location on the wafer.
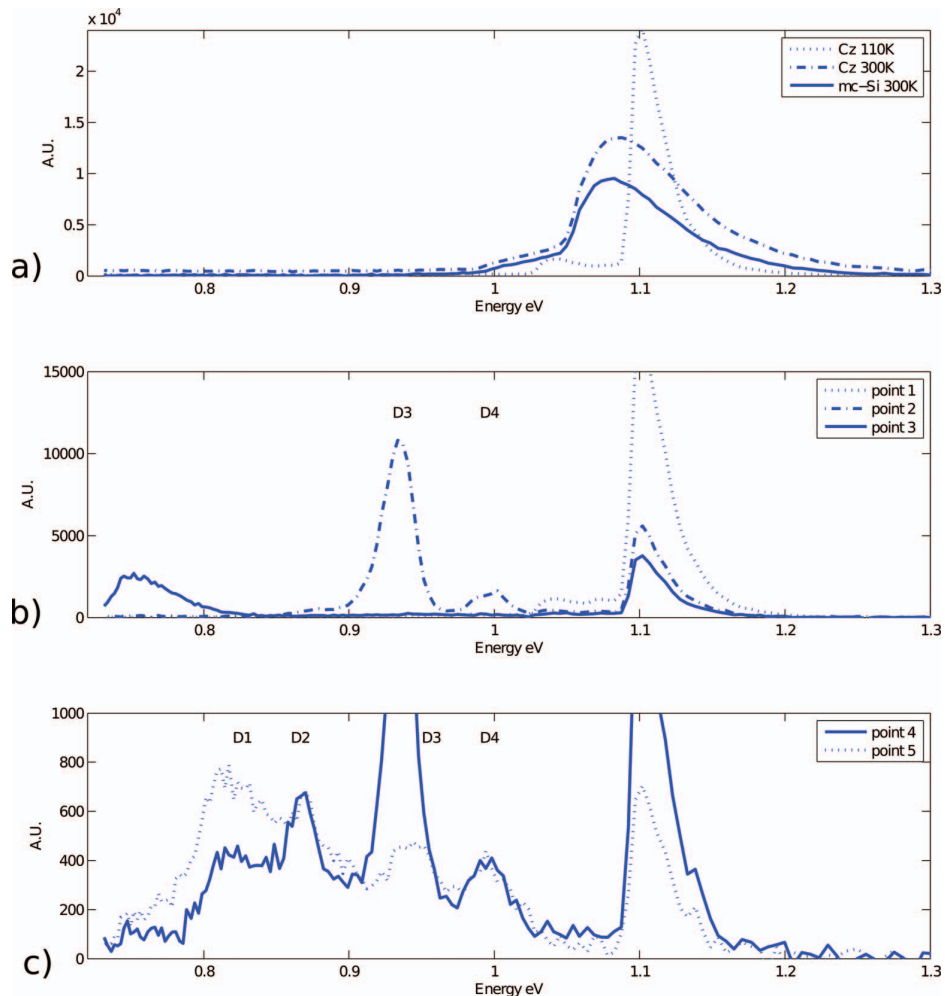
FIG. 4. Recorded spectra from selected points on the wafers (locations shown in Figs 1 and 2) : Si band-to-band photolu-minescense in a reference monocrystalline (Cz) wafer at 300 K [Fig. 2(b)] and 110 K [Fig. 2(d)] compared with a the signal from uncooled mc-Si at 300 K [Fig. 2(a)] are displayed in (a). Individual spectra from the points 1, 2, 3, 4 and 5 are shown in (b) and (c). The locations of the D-band lines (D1: 0.82 eV, D2: 0.87 eV, D3: 0.93 eV, D4: 1.0 eV) are indicated.

Spatial (x and y) and spectral (eV) visualization of the mc-Si wafer, imaged in Figure 5, reveals the extension of the crystal imperfections. The 3D cube is viewed from different angles to enhance the visualization. The BB PL emission and two layers of phonon replicas can be seen as well as the inter-band-gap emission in the wafer. Each emission exhibits characteristic distributions both in the spatial and spectral dimension. Luminescence from point- like features with sharp onset and end are evident as is emission with more diffuse nature.

IV. DISCUSSION

The D1 and D2 emissions do not occur physically together with D3 and D4 [Figs. 3(a) and 3(b)], supporting the theory that the D1/D2 pair and the D3/D4 pair have different origins. Most of the D1 and D2 emissions [Fig. 3(a)] originates from the lower right corner and along the right edge of the wafer, a region clearly anticorrelated with the BB PL signal [Fig. 2(c)]. It has been suggested that D1 and D2 have the same origin[12] but due to variations in the intensity ratio between the lines [see
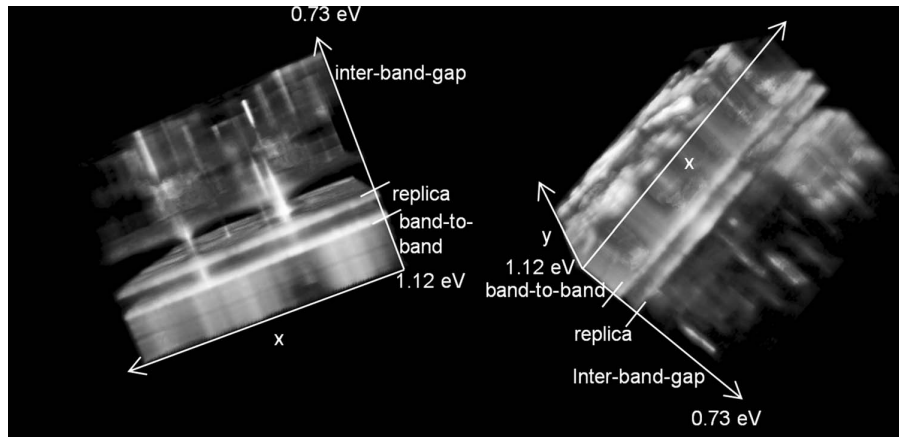
FIG. 5. Visualization of the recorded photoluminescense signals in the region 1.30 to 0.73 eV over the plane of a multicrystalline wafer in 2 (x-y) + 1 (energy) dimensions. The data set is viewed from two different angles. The emission energies due to band-to-band recombination with its two recorded phonon replicas as well as the emission from inter-band gap recombination through traps are indicated.

Figs. 4(b) and 4(c)], D1 is probably not the phonon replica of D2[4]. Although D1 and D2 generally occur together in our images, the D2 emission has a more diffuse character than D1. Moreover, there are several points detected in D1 and not in D2, and vice versa unlike results reported by Schubert *et al.*[13] This suggests that D1 and D2 could have partly different origins. This could be due to e.g., metal components that segregate together in some regions but not as a general rule.

The D3 signal seems to originate from several parts on the wafer [Fig. 3(b)] with a diffuse character. The D4 signal, also on Fig. 3(b) is very different from D3 but has similarities to parts of the D2 emission [Fig. 3(a)]. There are also very strong variations in the intensity ratio between the D3 and D4 line in the spectra from different locations [see for example the ratios in Figs. 4(b) and 4(c)]. These measurements opposes to Sekiguchi *et al.*[4] who suggested that D3 and D4 have the same origins. In addition to the D1 – D4 lines, an emission line at 0.75 eV was detected in the cooled mc-Si wafer [Fig. 3(c)]. The image in this wavelength region displays strong emission from points and small clusters distributed over the wafer. Some of these points coincide with points seen in the D1 emission indicating that the signal originates from components clustered on the same locations as those emitting in the D1. We note however that the common signal in D1 and D2 (the clusters in the lower right corner and along the right edge) is completely absent in the 0.75 eV image.

The recordings of the mc-Si wafer cooled to 110 K reveal emission lines that have previously only been detected at significantly lower temperatures in the range 5 – 20 K.[3,14,15] The D-lines described above have previously been detected in intentionally dislocation-induced Cz-wafers by PL and cathodoluminescence respectively.[14,15] However, in spite of the high sensitivity of our recordings, no emission lines could be detected in the Cz-Si wafer, other than the BB signal. This shows that the photoluminescence killers in Cz-Si - generally believed to be due to dislocation clusters around interstitial oxygen[11] are either absent in this as-grown sample or not radiatively active at the temperatures used for our recordings. The D-band emission lines observed in intentionally deformed crystals are hence most probably caused by changes due to the deformation and not by as-grown defects.

V. CONCLUSION

Hyperspectral imaging is a non destructive, highly sensitive macroscopic technique for PL imaging of Si wafers. Radiatively active emission due to crystal imperfections are clearly distinguished from the dominating band-to-band emission across the surface of the wafer, revealing the extensions of all the emission signals, both in the spatial and in the spectral dimension. The images

and spectra of our mc-Si sample display the four D-band emission lines and an additional emission at 0.75 eV, previously not reported. Based on our measurements, we suggest that all the emission D-lines could have different origins. Methods of analysis such as dislocation mapping, scanning electron microscopy (SEM), transmission electron microscopy (TEM) and confocal imaging will be the subject for further study.

[1] M. C. Schubert, J. Schön, P. Gundel, H. Habenicht, W. Kwapil, and W. Warta, J. Electron. Mater. **39**(6), 787 (2010).

[2] M. Seibt, R. Kahlil, V. Kveder, and W. Schroter, Appl. Phys. A - Mater. Science & Processing **96**(1), 235 (2009).

[3] T. Arguirov, W. Seifer, G. Jia, and M. Kittler, Semiconductors **41**(4), 436 (2007).

[4] T. Sekiguchi and K. Sumino, *Proceedings of the 18th International Conference on Defects in Semiconductors (ICDS-18)*, Sendai, Japan, p. 1201 (1995).

[5] M. Tajima, M. Ikebe, Y. Ohshita, and A. Ogura, J. Electron. Mater. **39**(6), 747 (2010).

[6] T. Trupke, R. A. Bardos, M. C. Schubert, and W. Warta, Appl. Phys. Lett. **89**, 044107 (2006).

[7] T. Trupke, E. Pink, R. A. Bardos, and M. D. Abbot, Appl. Phys. Lett. **90**, 093506 (2007).

[8] J. A. Giesecke, M. C. Schubert, B. Michl, F. Schindler, and W. Warta, Sol. Energy Mater. Sol. Cells **95**, 1011 (2011).

[9] B. Michl, M. Rüdiger, J. A. Giesecke, M. Hermle, W. Warta, and M. C. Schubert, Sol. Energy Mater. Sol. Cells **98**, 441 (2012).

[10] E. Olsen, and A. S. Flø, Appl. Phys. Lett. **99**, 011903 (2011).

[11] M. Ma, T. Ogawa, M. Watanabe, and M. Eguchi, J. Crystal Growth **205**, 50 (1999).

[12] M. Inoue, H. Sugimoto, M. Tajima, Y. Ohshita, and A. Ogura, J. Mater. Sci. - Materials in Electronics **19**, 132 (2008).

[13] M. C. Schubert, P. Gundel, M. The, W. Warta, M. Romero, S. Ostapenko, and T. Arguirov, *Proceedings of 23rd EUPVSEC*, Valencia, Spain, 17 (2008).

[14] H. Sugimoto, M. Inoue, M. Tajima, A. Ogura, and Y. Ohshita, J. Appl. Phys. Part 2-Letters & Express Letters **45**, 24-28, L641 (2006).

[15] H. Sugimoto, K. Araki, M. Tajima, T. Eguchi, I. Yamaga, M. Damrin, K. Kamisako, T. Saito, J. Appl. Phys. **102**, 054506 (2007).

Paper 3

Characterization of silicon wafers for photovoltaic applications using hyperspectral imaging

A. Flø[1], I. Burud[1], K.Kvaal[1], G. Stokkan[2], E.Olsen[1].

[1] Norwegian University of Life Sciences, Dept. Mathematical Sciences and Technology

[2] SINTEF Mat & Chem, NO-7465 Trondheim, Norway

Abstract

Multicrystalline Silicon wafers for solar cell applications has been studied with a hyperspectral camera (900-2500 nm) with the aim of characterizing bad areas in the wafer, causing reduced efficiency in the solar cell. This technique yields a spectrally resolved image of all radiative emission, in addition to a photoluminescence image of the band-to-band emission in silicon. The latter can be directly compared with a lifetime map of the excited carriers, which is validated by a carrier density image of one of our samples. A demonstration of Multivariate Curve Resolution on the hyperspectral data set showed that the loadings correspond well with previously studied emission signals in the wafer. Since the imaging procedure is non destructive and the Multivariate Curve Resolution provides a fast analysis we suggest that this technology could be implemented as a real time process line for characterization of multicrystalline wafers.

Keywords: Hyperspectral Imaging, Principal Component Analysis, Multivariate Curve Resolution, Solar Cells, Photoluminescence, Photoluminescence Imaging, Carrier Density Imaging

Introduction

In the photovoltaic industry, the use of multicrystalline silicon wafers is favoured by its low cost compared with monocrystalline wafers that are produced from one single crystal. However, for multicrystalline wafers one needs to deal with crystal imperfections like impurities and dislocations, reducing significantly the efficiency of the solar cell. Much effort is therefore dedicated to understanding how crystal imperfections in multicrystalline silicon appear, how they influence the cell efficiency and not the least, how they can be avoided or reduced. Photoluminescence (PL) imaging is a well-established, non-destructive technique for characterizing multicrystalline silicon wafers[1, 2]. The main principle is to excite electrons in the Si with a laser, and the radiative recombination of these electrons is followed by the

1

emission of the photoluminescence signal. A mechanism for recombination across the Si energy gap is the so-called radiative band-to-band signal (see Fig. 1a). In presence of crystal imperfections the band-to-band recombination will be perturbed and the electrons will follow alternative routes through traps in the bandgap (Fig. 1b). This process is called Shockley Read Hall recombination and can be visualized across the wafer as dark regions in a photoluminescence image since the signal in the band-to-band energy is very low. Shockley Read Hall[3] recombination may also be radiative, with emission at other energy levels than the band-to-band emission. Study of the spectral behavior across the wafer may therefore reveal information regarding the origins of the imperfections and how they influence the recombination routes in the energy band gap. Traditionally, spectral information has been obtained only from selected points on the wafer through NIR spectroscopy (e.g. [4] Inoue et al.). Recently we have demonstrated that both spatial and spectral information across the whole wafer could be obtained simultaneously using hyperspectral photoluminescence imaging[5]. This technique has been further explored to study the shape and structure of radiatively active recombination routes from crystal imperfections in the silicon wafer[6].

A hyperspectral camera collects the data in a three-dimensional data matrix, also known as a hypercube[7]. All the spectral channels are collected on top of each other to form a hypercube with two spatial axes (m and m pixel coordinates) and one spectral dimension (λ). Hyperspectral imaging has been used much in airborne and satellite images[8], and recently, several examples of hyperspectral imaging in laboratory studies have demonstrated the power of this technique for a large number of applications (e.g., [9,10]). In the present work hyperspectral imaging is conducted on multicrystalline Si wafers. In particular, we will explore if multivariate analysis like Multivariate Curve Resolution (MCR) of the data set could be used as an automated method to extract radiative emission from Si and crystal imperfections across the sample.

Experimental

Data aquisition
The samples were three surface passivated (a-Si:H), p-doped multicrystalline silicon wafers with dimension 50 x 50 mm. RGB images of the samples at room temperature are displayed in Fig. 2. The samples were cooled to 80 K since this reduces the band-to-band recombination in silicon, increases the population of excited charge carriers and thus enhances the signal from radiative crystal imperfections. The samples were cooled on an aluminum surface on top of a cryogen cooler filled with liquid nitrogen.
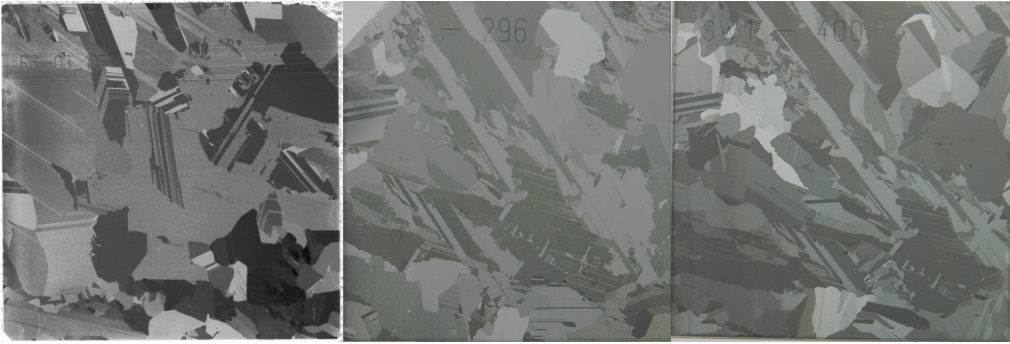
Fig 2. RGB images of the three studied Si wafers at room temperature.

The hyperspectral imaging experimental setup is shown in Fig. 3 and shows the hyperspectral camera, a cryogenic cooler, the sample, and a laser (Lasiris Magnum II, 808 nm) that was used as excitation source. The NIR hyperspectral images were recorded using a Specim SWIR camera. The size of the detector is 320 x 256 pixels. The camera has an HgCdTe detector and a spectral range from 900 nm to 2500 nm, distributed on 256 channels. One dimension of the detector is used for the spectral separation and the other for imaging one of the two spatial directions so that one line is recorded each time with a spectrum in each pixel. The second spatial dimension is obtained by moving the sample under the camera with a translation stage. It typically takes 4 seconds to scan the sample and the spatial resolution of the setup was of the order of 200 μm. An 850 nm low-pass optical filter was added to the focusing optics to remove scattered radiation from the laser leading to 2nd order harmonics detectable by the camera.
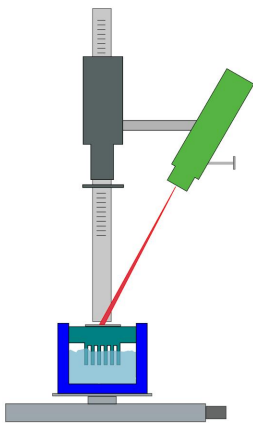

Figure 3. Sketch of the instrumental setup of VNIR camera, laser and cryogen holder for the sample.

In addition to the hyperspectral imaging, Carrier Density Imaging (CDI) was carried out for one of the wafers as an independent measurement technique to validate our technology. CDI is a well known spatially resolved carrier lifetime measurement technique in solar cell production, providing the actual local lifetimes of the excited

carriers[10]. Given that the CDI is carried out at 330K, a hyperspectral recording was also obtained at 330K for the same wafer.

Image processing

Dark frames of the detector were obtained by closing the aperture and capture 100 frames with the same exposure time as the sample frames. These were averaged and subtracted from the raw frames. The images contain a wafer in the center surrounded by the aluminum surface that is also seen as a background beneath the wafer. This background signal was subtracted by averaging the pixel columns on each side of the wafer for all spectral channels.

A contrast image was extracted from the hypercube by averaging the signals for selected wavelengths.
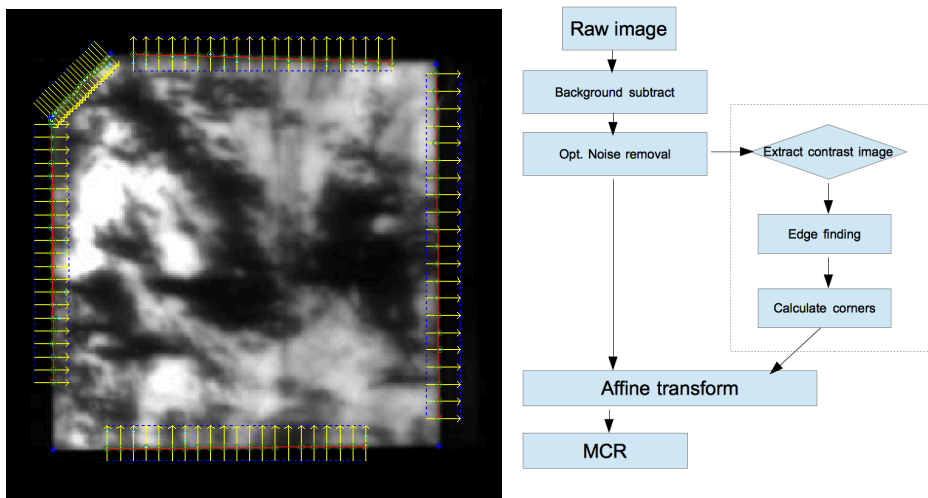

Fig 4a) Contrast image with edge detection algorithm, b) workflow of the data analysis.

By analyzing the edges in the contrast image (wafer) and the CDI image, the coordinates of the corners were determined by the crossing point of the lines from the edges. The directions of the search path in the edge finding algorithm, is indicated by the arrows in Fig. 4a). The crossing points were used in an affine transform for each wavelength to align the hypercube into a common coordinate system. For visualization of the band-to-band photoluminescence signal, the bands corresponding to 1130nm +- 2 bands were extracted from the aligned hypercube. A workflow of the alignment process is displayed in Fig. 4b).

Data analysis

Multivariate curve resolution (MCR) is an iterative resolution method that strives to recover the pure response profiles, such as spectra for hyperspectral images, of an unresolved mixture when no prior information is available about the nature and composition of these mixtures. MCR is based on a bilinear model, which requires a linear combination of the spectra of the pure components in the system. The bilinear

model is on the form $D = CSt + E$, where D is the raw measurement, C is the matrix of concentrations, called the scores matrix, and St the matrix of related pure spectra, called the matrix of loadings. E is the experimental error contained in the raw measurement[12]. Principal Component Analysis (PCA) is another useful tool to estimate the number of significant components in an image and to remove noise in large data sets[13]. PCA uses an orthogonal transformation to transform a data set with correlated variables into a set of values of linearly uncorrelated principal components. This transformation is defined in such a way that the first principal component has the largest possible variance and each succeeding component in turn has the highest variance possible under the constraint that it be orthogonal to the preceding components. Due to these constraints, PCA do not provide the true spectra and relative contribution profiles of the image constituents directly. This is why a wider refinement of PCA, the MCR, was chosen for the analysis in this work. The data matrix (D) is processed by iterations of the scores (C) and loadings (St). The number of components (physical constituents) contributing to D and to be modeled by MCR has to be determined. C and ST are optimized iteratively in an Alternating Least Squares (ALS) algorithm until convergence is reached. Diverse constraints may be applied in the process in order to obtain a physically meaningful solution.

The hypercube has to be unfolded to λ*(m x n) before the MCR can be performed. After the MCR analysis, the columns of the C matrix can be folded back to the height and width of the original image yielding a distribution map of each component of the analysis.

Results and discussion

The MCR analysis selects the band-to-band silicon photoluminescence signal as the first component and most dominant signal for all the three wafers. The other components consist of radiative recombination at other wavelength regions. The signals can be visualized in the loading plots and the score images from the MCR shown in Fig. 5 and 6, respectively. The loading plots are shown with energy (eV) on the x-axis, which allows us to directly compare them with the energy associated with the emission from crystal impurities. Common for the three wafers are the signals from four lines with energy peaks at 0.81, 0.88, 0.93 and 1.00 eV, commonly labeled D1 – D4, and generally believed to be related to dislocations in the crystal[13].
If MCR is to be used as a rapid method to extract radiative recombination in a hyperspectral image of a Si wafer it needs to agree with the manual selection of the physically known radiative signals. The comparison of the MCR result and the manually selected images from the datasets of one of the wafers, sample 2, is displayed in Fig 6. We note that the first component, MCR1, agrees well with the image of the band-to-band luminescence wavelength. The second component, MCR2, includes both D3 and D4. On the manually selected images in Fig. 6 we see that the

D3 and D4 signals are very correlated, which is most probably the reason why the MCR could not separate them. The third component, MCR3, corresponds to the D1 signal. We note that MCR does not extract the D2 signal. From the manually selected images it can be seen that D2 is very correlated to D3 and D4 for this wafer, which is probably the reason why MCR does not extract D2 as a separate signal. The fourth component, MCR4, agrees well with the manually selected signal from 0.75 eV.

Normally as a validation of the model, the model should be applied on a test set. Because of the nature of our samples and their uniqueness it is hard to get a good test set to validate the model. However we can evaluate the model visually.

For sample 1 there is an additional strong peak at 0.94 eV, also extracted with MCR (see loading plot Fig. 5a). This signal overlaps with D3 but has no signal in D4 and therefore seems to be due to a different mechanism than D3. A similar feature was found by Arguirov[14] and is referred to as the 'very high peak D3' signal. The origin of this signal will be the subject for further studies.

The band-to-band photoluminescence image obtained at 330 Kelvin gives a map of the local lifetimes of the excited carriers in the Si wafer. The high luminescent areas have high lifetime and are good regions providing high efficiency of the solar cell whereas dark areas are bad regions in the wafer where the Si band-to-band recombination is weak. This can be seen in Fig. 7 where the band-to-band photoluminescence image for sample 1 is compared with a CDI of the same wafer. CDI is known to give the actual lifetime of the excited carriers and could be used to calibrate the hypersepectral image and obtain lifetime maps directly from the photoluminescence images.

The band-to-band photoluminescence image for sample 1 is displayed in Fig. 8 with the radiative recombination signals from the crystal imperfections overlayed in red. This visualization maps the correlation between bad photoluminescent areas and emission from crystal imperfections. Using different colors for the various signals one could probe the radiative recombinations and see how each one relate to good and bad areas in the photoluminescence image.

Conclusion

Multivariate image analysis, and in particular, the MCR technique, seems very well suited to extract the individual signals from radiative recombination due to crystal imperfections in multicrystalline Si wafers for photovoltaic applications. Since the physics of the origin of the D-band emission lines is not yet fully understood, we cannot state whether the mixture of signals meets the criteria of MCR that the observed spectra is a linear combination of the spectra of the pure components. However, the results show good agreement with Arguirov[15] and Olsen and Flø[5]. Using

MCR one can split the well known D-band lines, the signal at 0.75 eV, and even the 'very high D3' signal from the band to band luminescence in a fast and efficient way.
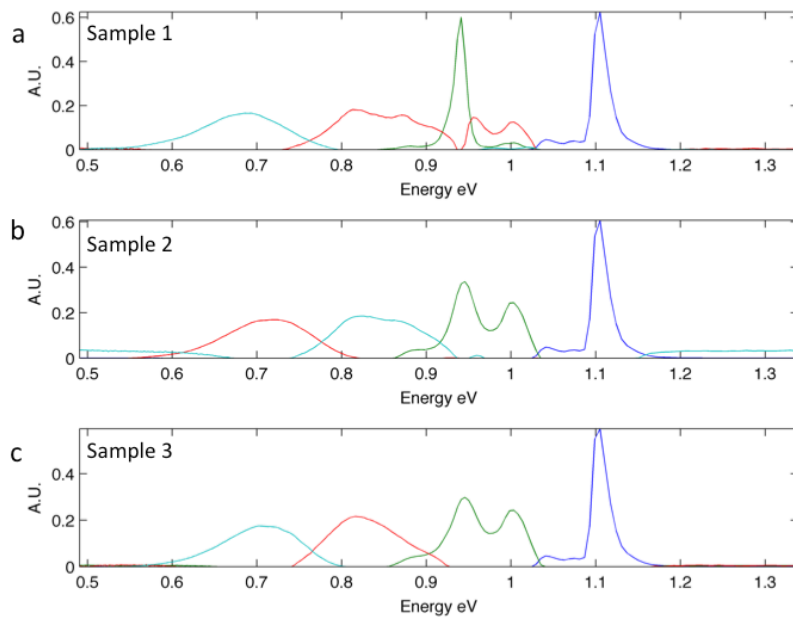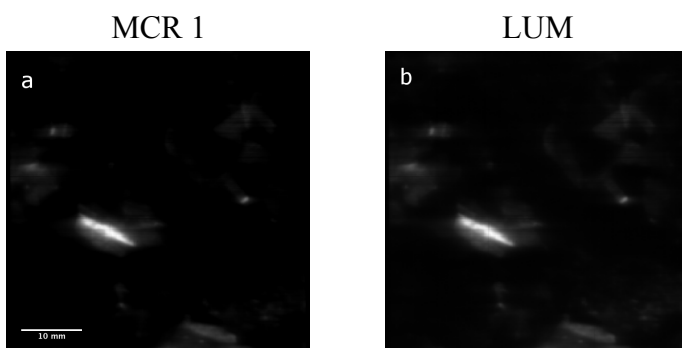

Figure 5: MCR loading plots for the three samples. The band to band emission is seen in blue at 1.1 eV together with the D-band lines. For sample 1 we see additional signal at 0.68 eV and the 'very high D3' line at 0.94 eV. For sample 2 and 3 we see the emission at 0.75 eV.
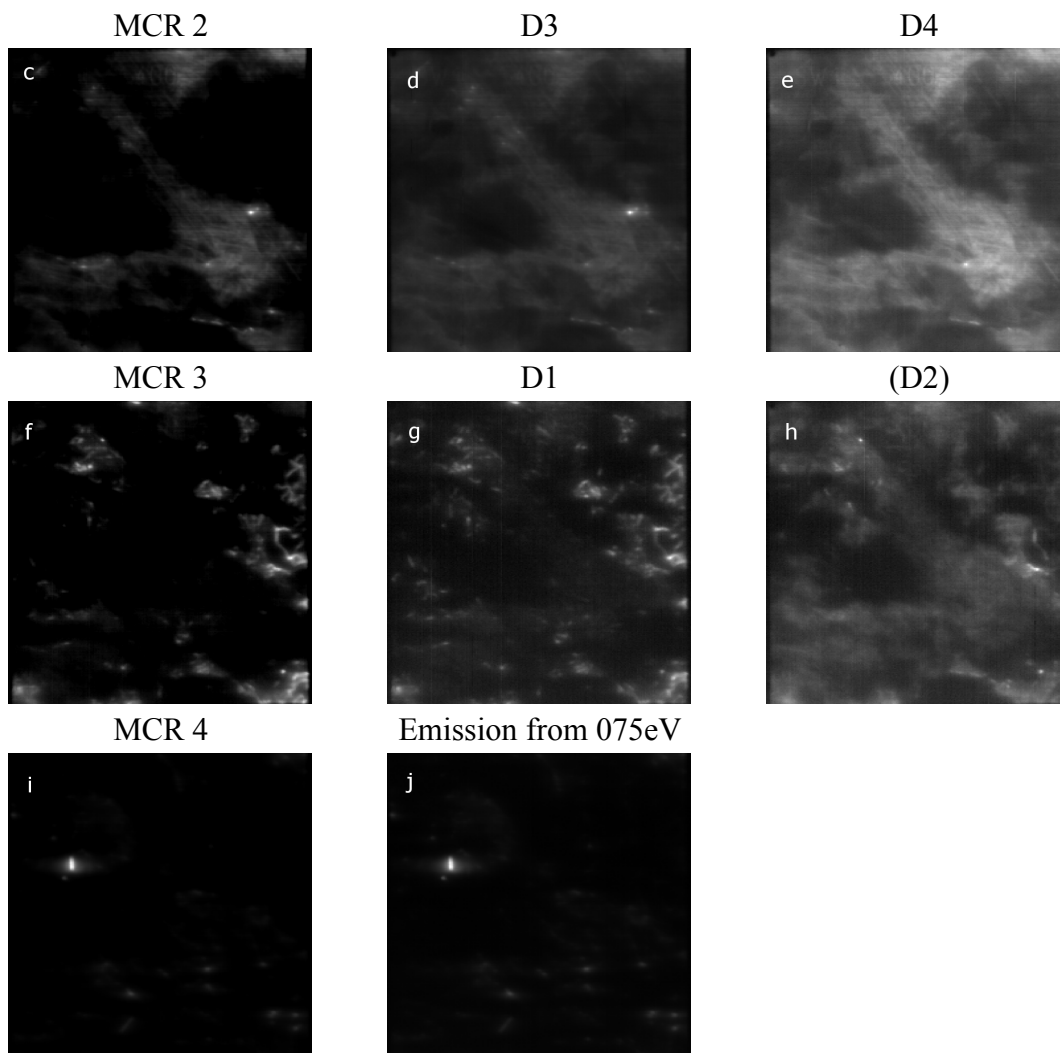
MCR 1   LUM

MCR 2	D3	D4
MCR 3	D1	(D2)
MCR 4	Emission from 075eV	

Figure 6: Left column MCR score plots and right columns, manually extracted wavelength. a) MCR score 1, b) Emission image band-to-band, c) MCR score 2, d) Emission image at 0.93eV (D3), e) Emission image at 1.0eV (D4), f) MCR score 3, g) Emission image 0.81eV (D1), h) Emission image at 0.88eV (D2), i) MCR score 4, j) Emission image at 0.75eV.
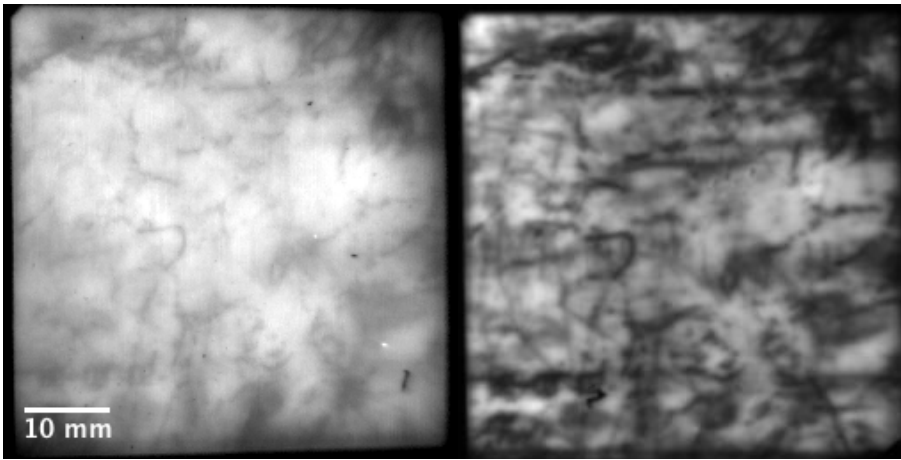
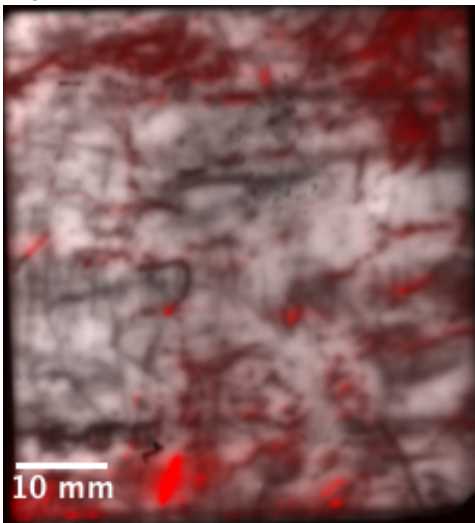Fig. 7: CDI measurement (left) and band to band photoluminescence image at 330 K (right)

Fig. 8: Spatially distribution of radiative emission. Band-to-band (white) and Shockley Read Hall recombination (red)

References

1. T. Trupke, R. A. Bardos, M. C. Schubert and W. Warta, Appl, Phys. Lett. 89, 044107 (2006).
2. T. Trupke, E. Pink, R. A. Bardos and M. D. Abbot, Appl, Phys. Lett. 90, 093506 (2007).
3. W. Shockley, W. Read, Physical Review, 1952, DOI: 10.1103/PhysRev.87.835
4. M Inoue, H Sugimoto, M Tajima, Y Ohshita, and A Ogura, J Mater. Sci: Mater Electron, Vol 19, p 132-134, (2008), doi: 10.1007/s10854-008-9605-5
5. E Olsen and A Flo, Appl Phys Lett, Vol 99, (2011)
6. I Burud, A Flo, and E Olsen, AIP, Vol 2, (2012)
7. J Burger, Hyperspectral NIR Image Analysis, Thesis, SLU, (2006)
8. A. Goetz et. al., Science Vol 228, Number 4704, 1985
9. Buddenbaum, H and Steffens, M, JSI, 2, 1 (2011)
10. Williams, P., Geladi, P., Fox, G., Manley, M. Analytica Chimia Acta 653, 121-130 (2009)
11. J Isenberg, S Riepe, S W Glunz, and W Warta, PVSC-02, pp.266-269, (2009), doi: 10.1109/PVSC.2002.1190509

12. S. Piqueras, L. Duponchel, R. Tauler, A. de Juan, Analytica Chemica vol. 705, pp:182-192, (2011), doi: 10.1016/j.aca.2011.05.020
13. Martens & Naes, Multivariate Calibration, 1989, ISBN-13: 9780471909798
14. T. Mchedlidze, T. Arguirov, O Kononchuk, M. Trushin and M. Kittler, Phys Stat Solidi C8 Nr 3 doi: 10.1002/pssc.201000367
15. Arguirov, Thesis, der Brandenburgischen Technischen Universität Cottbus, 2007

Paper 4

Distribution of radiative crystal imperfections through a silicon ingot

A. Flø,[1,a] I. Burud,[1] K. Kvaal,[1] R. Søndenå,[2] and E. Olsen[1]

[1]*Norwegian University of Life Sciences, Dept. Mathematical Sciences and Technology, P.O. Box 5003, 1432 Ås, Norway*
[2]*Institute for Energy Technology, Department of Solar Energy, P.O. Box 40, 2027 Kjeller, Norway*

Crystal imperfections limit the efficiency of multicrystalline silicon solar cells. Recombination through traps is more prominent in areas with high density of crystal imperfections. A method to visualize the distribution of radiative emission from Shockley Read Hall recombination in silicon is demonstrated. We use hyperspectral photoluminescence, a fast non-destructive method, to image radiatively active recombination processes on a set of 50 wafers through a silicon block. The defect related emission lines D1 and D2 may be detected together or alone. The D3 and D4 seem to be correlated if we assume that an emission at the similar energy as D3 (VID3) is caused by a separate mechanism. The content of interstitial iron (Fe_i) correlates with D4. This method yields a spectral map of the inter band gap transitions, which opens up for a new way to characterize mechanisms related to loss of efficiency for solar cells processed from the block. *© 2013 Author(s). All article content, except where otherwise noted, is licensed under a Creative Commons Attribution 3.0 Unported License.* [http://dx.doi.org/10.1063/1.4834155]

I. INTRODUCTION

A. Material defects

Several types of material defects can be found in multicrystalline silicon (mc-Si) for photovoltaic applications. Impurities are introduced with the feedstock material or by in-diffusion from the crucible, while grain boundaries and dislocations are formed during the crystal solidification process. These material defects may act as recombination sites for electrons and holes, reducing the minority carrier lifetime in the silicon which is an indicator of the quality of the wafers and the performance of the final solar cells. In multicrystalline silicon, the material defects are not homogenously distributed. Dislocation clusters, that are known to be highly detrimental to the minority carrier lifetime, tend to grow with increasing height in the ingot. Such dislocation clusters can be traced back to the origin, typically in a crystal defect.[1] Metallic impurities tend to agglomerate at grain boundaries or in dislocation clusters.[2] It is therefore important to study the spatial distribution and composition of crystal imperfections in a wafer in order to understand and reduce the performance limiting effects in solar cells. Traditionally, minority carrier lifetime of silicon wafers has been measured using quasi steady state photo conductance (QssPC) and microwave photoconductance decay (μ-PCD).[3] Photoluminescence imaging (PL) of the band-to-band (BB) emission of crystalline silicon at room temperature is a more recent approach for characterizing silicon wafers as well as solar cells.[4]

---

[a]Electronic mail: andreas.flo@umb.no

3, 112120-1

B. D-lines

There are several other radiative emission lines in silicon in addition to the BB recombination. Four radiative emission lines, believed to originate from dislocations in the crystals were first reported in 1976 by Drozdow *et al.*[5] These four lines are conventionally labeled D1, D2, D3 and D4 with energies 0.8 eV, 0.87 eV, 0.94 eV and 1.0 eV respectively. Several theories have been proposed for the origins of the D-lines and other radiative emissions from crystal imperfections, also called Defect Related Luminescence (DRL). It has been suggested by Sauer *et al.*[6] that D1-D4 are due to relaxed dislocations whereas Higgs *et al.*[7] suggest transition-metals as a source for the D-band emission lines. Further it is proposed by Ostapenko[8] that oxygen or heavy metals influence the half-width and intensity of D1. Sekiguchi and Sumino[9] associate D3 and D4 with slip lines and link D1 and D2 to intersections of plural slip lines. They also observed pairwise similarity between D1/D2 and D3/D4 regarding their spatial distribution. Oxygen precipitates has also been found to be a possible origin of the D-lines by Pizzini *et al.*[10] and Tajima *et al.*[11] Arguriov[12] proposed D1 and D2 to be generated by transitions between one-dimensional bands on 60° disclocations and that D3 and D4 are linked to dislocations decorated by metallic impurities. Recently Mchedlidze associates screw dislocations with a small twist angle to the D-lines and the edge dislocations to non radiative recombination.[13]

Investigation of DRL is mainly performed by laboratory-based spectroscopic point mapping methods, such as described by Mudryi *et al.*[14] and Ostapenko *et al.*[8] Recently single band methods using band pass filters on InGaAs cameras have been reported by Mankovics *et al.*[15] and Schmid *et al.*[16] Also hyperspectral technologies have been applied by Peloso *et al.*,[17] as well as by Olsen&Flo[18] and Burud *et al.*[19] The advantage of using hyperspectral imaging is that the entire spectrum is acquired at each point. Instead of selecting a priori regions for detailed studies with e.g. spectrometry, the relevant signals can be extracted by multivariate postprocessing from a full hyperspectral dataset.

In the present work we investigate DRL and BB luminescence through an ingot by selecting 50 wafers evenly distributed along the height of the ingot. These wafers are studied with a hyperspectral camera in order to map, both spatially and spectrally, the distribution of radiative emissions from material defects. Regular PL imaging and μ-PCD measurement were also carried out, the latter yielding a map of interstitial iron across the wafer. Hyperspectral PL images have been aligned and compared with the regular PL images and the interstitial Fe (Fe$_i$) maps. Two emission signals at 0.75 eV and 0.94 eV believed to be associated with point defects are investigated closer. Distribution of Fe$_i$ is shown compared to the D4 emission and BB image for selected wafers from the ingot.

II. EXPERIMENTAL DETAILS

A. Samples and preparation

Conventionally manufactured p-type mc-Si wafers with an initial thickness of 180 μm and resistivites from 1 to 1.5 Ωcm are studied. 50 wafers of size 156 × 156 were selected, evenly distributed along the height of a centre block of an ingot. The first few wafers are from the bottom red zone. After an HNA-etch (HF:Nitric acid:Acetic acid) and a subsequential cleaning, the wafers were surface passivated using hydrogenated amorphous silicon (a-Si:H) deposited by plasma enhanced chemical vapor deposition PE-CVD. The final thickness of the wafers was 164 μm. From these wafers, 50 × 50 mm large samples were cut from the corner corresponding to the lower left corner of the center block. These were characterized using BB PL-imaging (LIS-R1 from BTI), μ-PCD (WT-2000PV from Semilab) as well as hyperspectral imaging. Hyperspectral images of the samples were obtained using a SWIR MCT camera (Specim, Oulu, Finland) covering the wavelength region 926-2527 nm (0.49-1.34 eV). A line laser with wavelength 808 nm and irradiated power density of approximately 2 W/cm^2, was employed as excitation source. Our setup yields spatial and spectral resolutions of 200 μm and 6 nm, respectively. The experimental setup is shown in Fig. 1. Hyperspectral images were obtained of the wafers at 300 K and 80 K. The samples were cooled on a cryogenic cooler filled with liquid nitrogen. Scanning one sample takes typically 3-4s but can be optimized for in-line use.
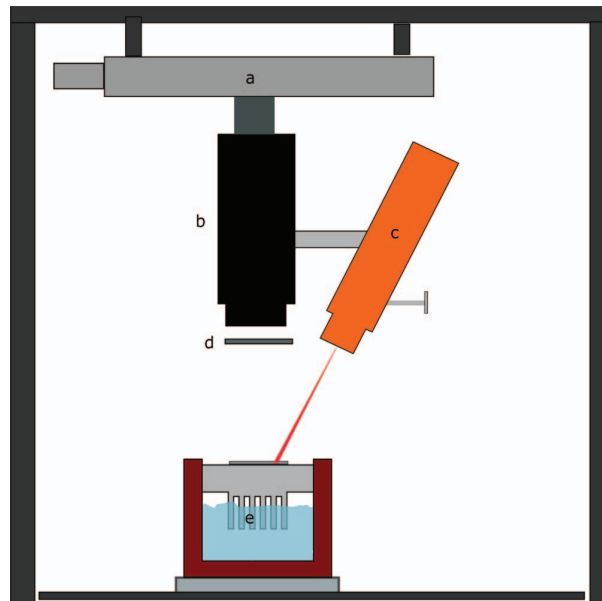
FIG. 1. Experimental setup showing a) the translation stage, b) the hyperspectral camera, c) the line laser, d) the filter and e) the cryogenic cooler.

B. Data processing

To compare the hyperspectral images with the PL-images and the Fe$_i$ maps, an alignment of the data was performed. Some preprocessing steps were needed for this purpose. A hyperspectral camera collects the data in a three-dimensional data matrix, also known as a hypercube.[20] The raw images have low contrast at the edges of the wafer since the luminescence is not homogeneously distributed. To find corresponding points in both the hyperspectral images and complementary measurements (μ-PCD and conventional PL), several selected wavelengths/channels were extracted from each hypercube to create images with high contrast where the corners could be easily selected as reference points. The complementary measurements were contrast adjusted to locate the corresponding points. All the datasets, hypercubes and complementary measurements were then transformed with an affine transform to a common coordinate system.

Multivariate Curve Resolution (MCR) was used to extract the most important signals from the hypercube in a fast and efficient way. A hyperspectral cube can comprise thousands of spectra, many of them highly correlated. It is therefore useful to apply mathematical techniques to extract the desirable information. MCR is a common method within multivariate statistics for reducing the dimension of large data sets.[21] An MCR analysis reduces the hyperspectral data cube into a certain number of components containing all significant signals in the hypercube. These can be visualized through so called score images and loading plots for each component. Applied to PL imaging of silicon wafers the loading plot yields directly the significant spectral features across each wafer.

III. RESULTS AND DISCUSSION

A. Emissions

All the hyperspectral images were analyzed using MCR in order to extract the significant emissions in the data cubes. The cubes of 256 images were reduced to 4-5 components. The combined loadings from all the MCR components are displayed in Figs. 2 and 3 for wafer #3 and #50 respectively in order to illustrate the top and bottom of the ingot. The loadings are plotted with
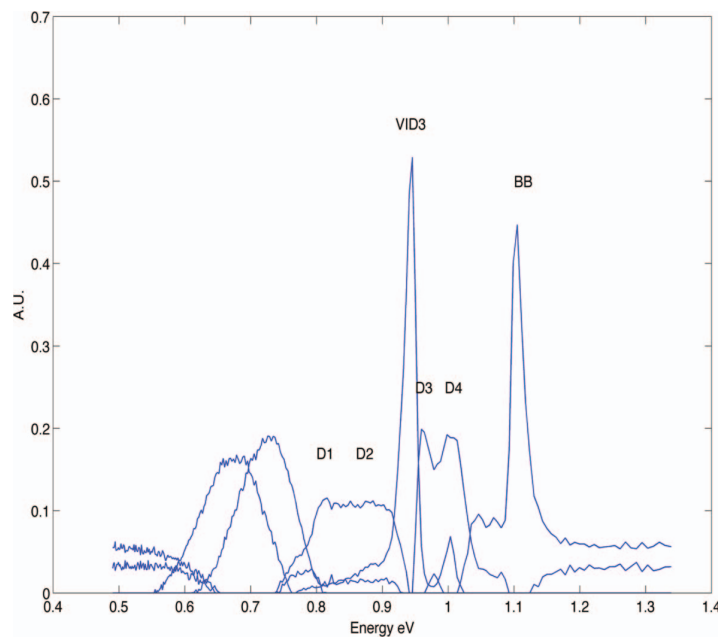
FIG. 2. MCR loadings for wafer #3. The BB emission peak is clearly extracted at 1.1 eV, the D3 and D4 appear as blended peaks, the VID3 appears as a high independent peak, the D1 and D2 are not well separated. Emissions at 0.68 eV and 0.7 eV are extracted as individual peaks.
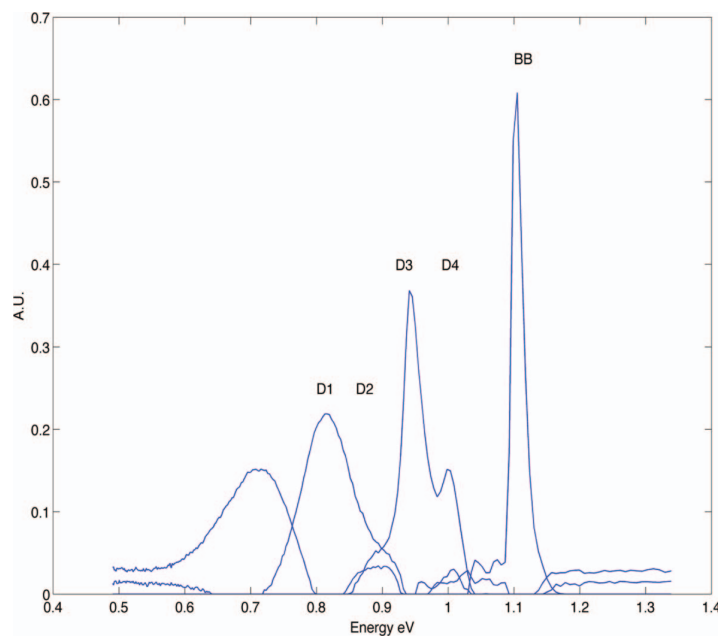

FIG. 3. MCR loadings for wafer #50. The BB emission peak is clearly extracted at 1.1 eV, the D3 and D4 appear as blended peaks, VID3 is also blended with D3. D1 and D2 are blended. Emission 0.7 eV is extracted as one individual peak but with a tail to the lower energy region.
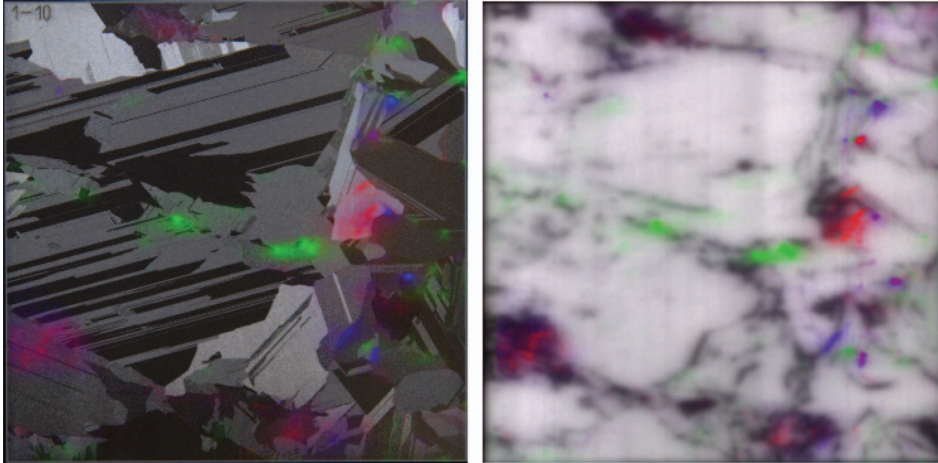
FIG. 4. RGB photographical image (left) and PL - image (right) of wafer #10 (50 mm $\times$ 50 mm) with D1 (red), D2 (blue) and emission from 0.75 eV (green) overlaid.
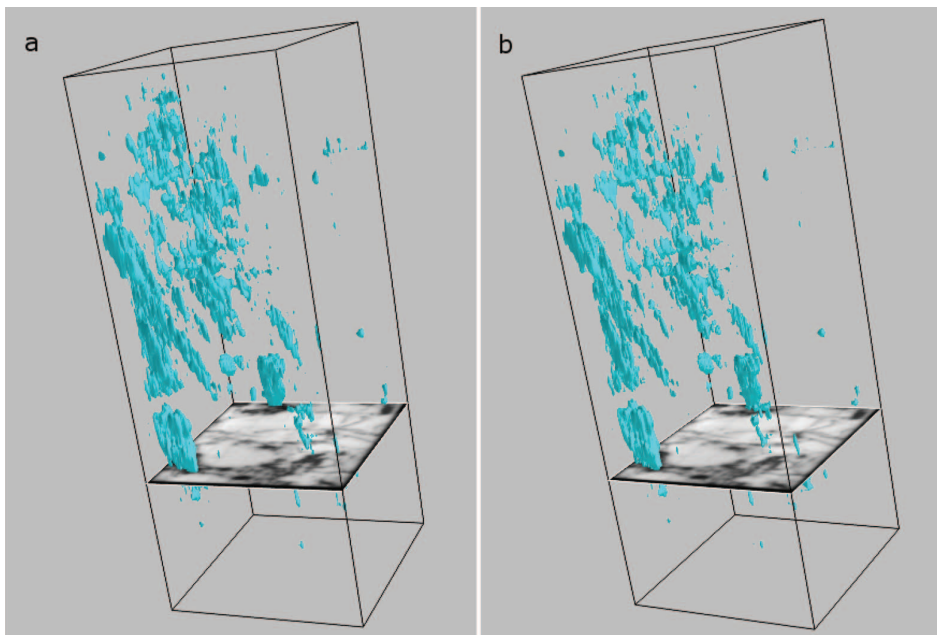

FIG. 5. A 3D model of a) the D1 emission (blue) and b) the D2 emission (blue) through the height of the ingot. The amount of D1 and D2 emission remains quite stable towards the top of the ingot. The D1 and D2 mostly coexist through the ingot. A PL-image is shown at 25% solidification.

eV on the x-axis for direct comparison with the spectral behaviour of the different mechanisms. The signals from the BB emission in silicon at 1.1 eV and the four known D-lines can easily be identified in the figures. The emissions from D3 (0.94 eV) and D4 (1.0 eV) are resolved as one phenomenon with MCR for both wafers. This corresponds well with previous reports stating that they have the same origin, and that D3 is a phonon replica of D4.[12,22] The MCR reveals a strong and sharp signal at 0.93-0.94 eV in wafer#3, hereafter called '*very intense D3*' (VID3). This signal has also been reported by Arguirov,[12] and the origin of this signal will be discussed below in subsection (III B).
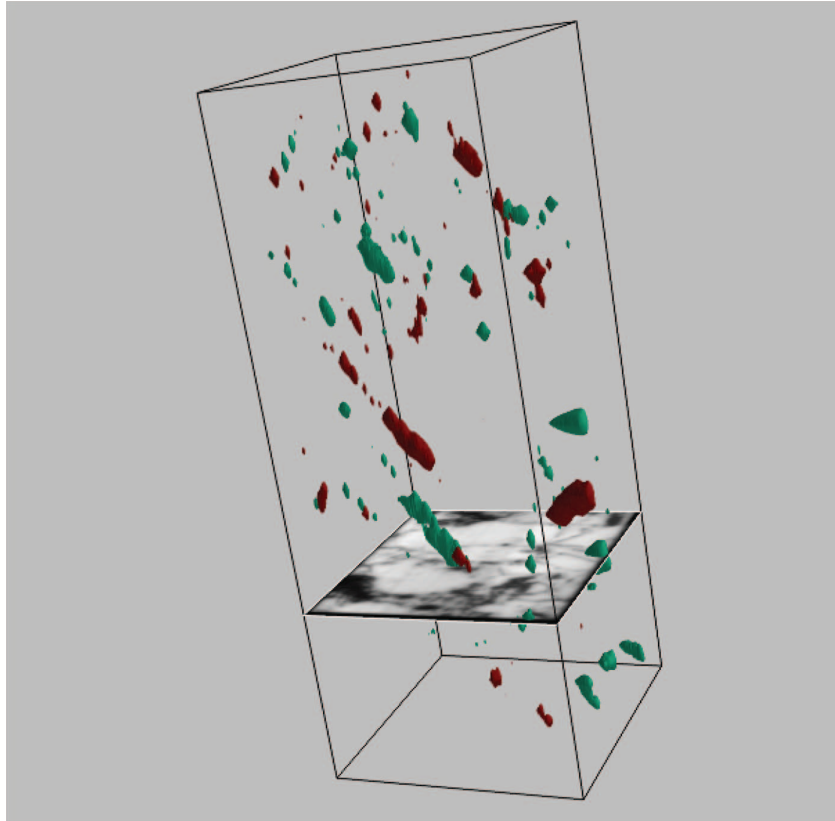
FIG. 6. 3D visualization of the mc-Si block. The dimensions of the studied volume are $50 \times 50 \times 200$ mm extracted from lower left corner of the center brickof the ingot as described in the text in IIA . Emission from VID3 (red) and emission from 0.75 eV (blue) are displayed along the heigh of the block. The BB PL image is inserted for wafer corresponding to 25% solidification.

Although not clearly resolved for wafer#50, the strong D3 signal for this sample indicate that this peak is a blend of D3 and VID3. This also fits into the theory of D3 being a phonon replica of D4 since that implies that their intensity ratio is constant. This is only compatible with our data under the assumption that the D3 for wafer#50 is a blend of D3 and VID3.

For the two samples #3 and #50, D1 and D2 seem to always appear together. This can be seen from the MCR loading plots in Figs. 2 and 3. However, D1 and D2 do not always coexist, as is shown for wafer#10 in Fig. 4. An RGB image and a BB PL image of the wafer is displayed with the emissions from the energies 0.8 eV (D1), 0.87 eV (D2) and 0.75 eV overlaid in different colors. Spatial variation of D1/D2 is also reported by Arguirov.[12] Although it is often stated that D1 and D2 correlate with dislocation clusters, our results indicate that the amount of D1 and D2 does not change much towards the top of the ingot (Fig. 5) although the lifetime goes down and the dislocation intensity increases.

A broad signal with a peak at 0.75-0.76 eV is separated from another broad peak at 0.68 eV for wafer#3 that are not present in wafer#50 (Fig. 2 and 3). In wafer #50, there is, however, an emission with peak at 0.7 eV. These three peaks appear at the same spatial locations in the ingot and could be caused by the same defect. However, impuritites tend to accumulate in and near grain boundaries and dislocations, and several different defects could therefore coexist in the same location. The 3-dimensional visualization of these signals in Fig. 6 indicate that they are point defects spread out in the ingot. The points seem to be mainly located at grain boundaries, as shown in Fig. 4. An emission from 0.75-0.78 eV was previously reported to be caused by oxygen precipitates.[10,23]
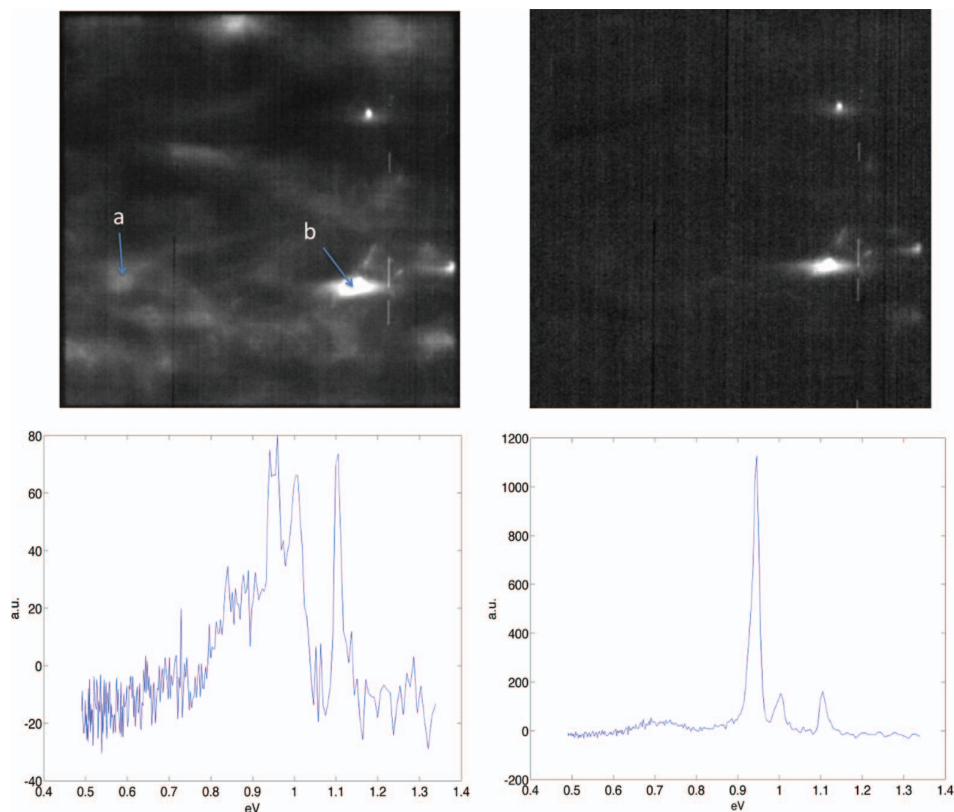
FIG. 7. Top left: Image of D3 wafer in #4, Top right: Image of very intense D3 (D3-D4), Lower left: Spectrum in point a, Lower right: Spectrum of very intense D3 spot in point b.

B. Very intense D3

The high peak emission from 0.94 eV, VID3, radiate the similar energy as D3, but with different distribution and properties. This has been reported by Arguirov,[12] Bradfield *et al.*[24] and Brown *et al.*[25] In order to study the spatial distribution of VID3 we define it as the difference image between the emission D4 and D3 (displayed in Fig. 7). The distribution through the ingot is shown in Fig. 6. As shown in Fig. 7(a) the relation between D3 and D4 is quite stable over the wafer except for some points in Fig. 7(b).

C. FeB mapping

The bulk [Fe$_i$] has been studied by FeB-pair splitting comparing the lifetime before and after illumination using μ-PCD. The amount of interstitial iron was determined using:

$$[Fe_i] = C_{\mu-PCD}(\frac{1}{\tau_{after}} - \frac{1}{\tau_{before}}) \tag{1}$$

Where C$_{\mu-PCD}$ = 3.4e13 μs/cm^3. The distribution of interstitial iron in wafer #10 and wafer #45 are shown in Fig. 8. The first few wafers are from the bottom red zone of the ingot and are expected to contain significant amounts of iron. Wafer #10 lies well above this bottom red zone. Due to segregation, an increase in the iron concentration is expected towards the top of the ingot (last to solidify). In addition, the dislocation density increases towards the top of the ingot.[1] Minority carrier lifetime maps show a higher average lifetime in wafer #10 than in wafer #45, mainly due to the increased dislocation density in wafer #45. Iron tend to agglomerate at grain boundaries
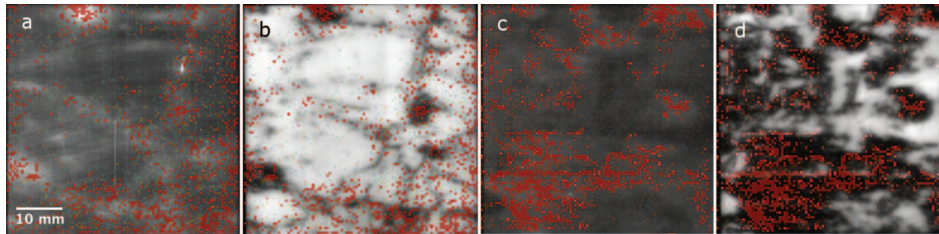
FIG. 8. The D4 signal and the PL-image of wafer #10 are shown in a) and b), while c) and d) show wafer #45. The concentrations interstitial iron is overlaid (red). A high D4 signal (bright) correspond well with a low BB signal in the PL-image as well as a high Fe_i-concentration. (Note: Fe_i intensity scale is different for wafer #10 (2e10cm^{-3}) vs. wafer #45 (10e10cm^{-3})

and dislocations contributing to the increased iron content towards the top. More iron is therefore expected in wafer #45 than in wafer #10. Fig. 8(a) shows the correlation betwen the D4 line and the iron concentration from FeB-splitting. Both the D4 line and the Fe_i are mainly found at grain boundaries shown in Fig. 8(b). Figs. 8(c) and 8(d) show the same correlation for wafer #45. Larger dislocation clusters coincide with both a high Fe_i-content as well as a high D4-signal.

IV. CONCLUSION

Defect related luminescence with hyperspectral techniques is a fast non-destructive method to classify the different radiative defects in multicrystalline silicon wafers. Used on a set of wafers for a silicon block it provides information on the distribution of DRL in silicon. The luminescence with energy at 0.75 eV and 0.94 eV (VID3) are probably caused by point defects and is evenly distributed along the height of the block. The point defects are located at or near grain boundaries. The D1 and D2 lines has similar features, but do not always appear together. Our measurements indicate a correlation between FeB and D4. The D3 and D4 are correlated if VID3 is an independent feature as suggested. A bigger sample holder would reveal more information about dislocation growth. Analysis of wafers with known distribution of impurities will be the topic for further studies.

[1] B. Ryningen, G. Stokkan, M. Kivambe, T. Ervik, and O. Lohne, Acta Materialia **59**, 7703 (2011).
[2] D. MacDonald, A. Cuevas, A. Kinomura, Y. Nakano, and L. J. Geerligs, Journal of Applied Physics **97**, 033523 (2005).
[3] S. Rein, *Lifetime Spectroscopy: A Method of Defect Characterization in Silicon for Photovoltaic Applications* (Springer-Verlag, 2005).
[4] T. Trupke, B. Mitchell, J. W. Weber, W. McMillan, R. A. Bardos, and R. Kroeze, Energy Procedia **15**, 135–146 (2012).
[5] N. A. Drozdow, A. A. Patrin, and V. D. Tkachev, Pis'ma Zh. Exsp. Teor. Fiz **23**, 597 (1976).
[6] R. Sauer, J. Weber, J. Stolz, E. R. Weber, K. Küsters, and H. Alexander, Appied Physics A Solids and Surfaces (1984).
[7] V. Higgs, M. Goulding, A. Brinklow, and P. Kightley, Appl. Phys. Lett. **60**, 1369 (1992).
[8] S. Ostapenko, I. Tarasov, J. P. Kalejs, C. Haessler, and E.-U. Reisner, Semiconductor Science and Technology **15**, 840 (2000).
[9] T. Sekiguchi and K. Sumino, Journal of Applied Physics **79**, 3253 (1996).
[10] S. Pizzini, M. Guzzi, E. Grilli, and G. Borionetti, Journal of Physics: Condensed Matter **12**, 10131 (2000).
[11] M. Tajima, Y. Iwata, F. Okayama, H. Toyota, H. Onodera, and T. Sekiguchi, Journal of Applied Physics **111**, 113523 (2012).
[12] T. Arguirov, "Electro-optical properties of dislocations in silicon and their possible application for light emitters," Ph.D. thesis, der Brandenburgischen Technischen Universität Cottbus, Cottbus, Germany (2007).
[13] T. Mchedlidze, T. Arguirov, O. Kononchuk, M. Trushin, and M. Kittler, Phys. Status Solidi **8**, 991 (2011).
[14] A. V. Mudryi, F. P. Korshunov, A. I. Patuk, I. A. Shakin, T. P. Larionova, A. G. Ulyashin, R. Job, W. R. Fahrner, V. V. Emtsev, V. Yu. Davydov, and G. Oganesyan, Physica B: Condensed Matter **308-310**, 181 (2001).
[15] D. Mankovics, R. Schmid, T. Arguirov, and M. Kittler, Cryst. Res. Technol. **47**, 1148 (2012).
[16] R. P. Schmid, D. Mankovics, T. Arguirov, M. Ratzke, T. Mchedlidze, and M. Kittler, Physica Status Solidi (A) **208**, 888 (2011).
[17] M. P. Peloso, J. S. Lew, B. Hoex, and A. G. Aberle, Energy Procedia **15**, 171 (2012).
[18] E. Olsen, and A. Flø, Appl. Phys. Lett. **99** (2011).
[19] I. Burud, A. Flø, and E. Olsen, AIP **2** (2012).
[20] J. Burger, "Hyperspectral NIR Image Analysis," Ph.D. thesis, pub.epsilon.slu.se, Umeå, Sweden (2006).

[21] Piqueras, A selection of papers presented at the 12th International Conference on Chemometrics in Analytical Chemistry **705**, 182 (2011).

[22] K. Weronek, J. Weber, and R. Buchner, in *Polycrystalline Semiconductors II* (1991) pp. 50–55.

[23] S. Binetti, S. Pizzini, E. Leoni, R. Somaschini, A. Castaldini, and A. Cavallini, Journal of Applied Physics **92**, 2437 (2002).

[24] P. L. Bradfield and T. G. Brown, Physical Review B **38**, 3533 (1988).

[25] T. G. Brown, Appl. Phys. Lett. **49**, 245–247 (1986).